

SPHERICAL TREE-SLICED WASSERSTEIN DISTANCE

Anonymous authors

Paper under double-blind review

ABSTRACT

Sliced Optimal Transport (OT) simplifies the OT problem in high-dimensional spaces by projecting supports of input measures onto one-dimensional lines, then exploiting the closed-form expression of the univariate OT to reduce the computational burden of OT. Recently, the Tree-Sliced method has been introduced to replace these lines with more intricate structures, known as tree systems. This approach enhances the ability to capture topological information of integration domains in Sliced OT while maintaining low computational cost. Inspired by this approach, in this paper, we present an adaptation of tree systems on OT problem for measures supported on a sphere. As counterpart to the Radon transform variant on tree systems, we propose a novel spherical Radon transform, with a new integration domain called spherical trees. By leveraging this transform and exploiting the spherical tree structures, we derive closed-form expressions for OT problems on the sphere. Consequently, we obtain an efficient metric for measures on the sphere, named Spherical Tree-Sliced Wasserstein (STSW) distance. We provide an extensive theoretical analysis to demonstrate the topology of spherical trees, the well-definedness and injectivity of our Radon transform variant, which leads to an orthogonally invariant distance between spherical measures. Finally, we conduct a wide range of numerical experiments, including gradient flows and self-supervised learning, to assess the performance of our proposed metric, comparing it to recent benchmarks.

1 INTRODUCTION

Despite being embedded in high dimensional Euclidean spaces, in practice, data often reside on low dimensional manifolds (Fefferman et al., 2016). The hypersphere is one such manifold with various practical applications. The range of applications involving distributions on a hypersphere is remarkably broad, underscoring the significance of spherical geometries across multiple fields. These applications encompass spherical statistics (Jammalamadaka, 2001; Mardia & Jupp, 2009; Ley & Verdebout, 2017; Pewsey & García-Portugués, 2021), geophysical data (Di Marzio et al., 2014), cosmology (Jupp, 1995; Cabella & Marinucci, 2009; Perraudin et al., 2019), texture mapping (Elad et al., 2005; Dominitz & Tannenbaum, 2009), magnetoencephalography imaging (Vrba & Robinson, 2001), spherical image representations (Coors et al., 2018; Jiang et al., 2024), omnidirectional images (Khasanova & Frossard, 2017), and deep latent representation learning (Wu et al., 2018; Chen et al., 2020; Wang & Isola, 2020; Grill et al., 2020; Caron et al., 2020; Davidson et al., 2018; Liu et al., 2017; Yi & Liu, 2023).

Optimal Transport (OT) (Villani, 2008; Peyré et al., 2019) is a geometrically natural metric for comparing probability distributions, and it has received significant attention in machine learning in recent years. However, OT faces a significant computational challenge due to its supercubic complexity in relation to the number of supports in input measures (Peyré et al., 2019). To alleviate this issue, several variants have been developed to reduce the computational burden, including entropic regularization (Cuturi, 2013; Scetbon et al., 2021), minibatch OT (Fratras et al., 2019), and the Sliced-Wasserstein distance (Rabin et al., 2011; Bonneel et al., 2015).

Related work. There has been growing interest in utilizing OT to compare spherical probability measures (Cui et al., 2019; Hamfeldt & Turnquist, 2022). To mitigate the computational burden, recent studies have focused on sliced spherical OT (Quellmalz et al., 2023; Bonet et al., 2022; Tran et al., 2024a). Quellmalz et al. (2023) introduced the vertical slice transform and a normalized

version of the semicircle transform to define sliced OT on the sphere. The semicircle transform was also employed in (Bonet et al., 2022) to define a spherical sliced Wasserstein. Meanwhile, Tran et al. (2024a) utilized stereographic projection to create a spherical distance between measures via univariate OT problems. However, projecting spherical measures onto a line or circle poses challenges due to the loss of topological information. Furthermore, comparing one-dimensional measures on circles is computationally more expensive, as it requires an additional binary search.

Tran et al. (2024b) offers an alternative method by substituting one-dimensional lines in the Sliced Wasserstein framework with more complex domains, referred to as tree systems. These systems operate similarly to lines but with a more advanced and intricate structure. This approach is expected to enhance the capture of topological information while preserving the computational efficiency of one-dimensional OT problems. Inspired by this observation, we propose an adaptation of tree systems to the hypersphere, called spherical trees, to develop a new metric for measures on the hypersphere. Spherical trees satisfy *two important criteria*: (i) spherical measures can be projected onto spherical trees in a meaningful manner, and (ii) OT problems on spherical trees admit a closed-form expression for a fast computation.

Contribution. Our contributions are three-fold:

1. We provide a comprehensive theoretical construction of spherical trees on the sphere, analogous to the notion of tree systems. We demonstrate that spherical trees, as topological spaces, are metric spaces defined by tree metrics, which ensures that OT problems on these spaces can be analytically solved with closed-form solutions.

2. We propose the Spherical Radon Transform on Spherical Trees, which transforms functions on the sphere to functions on spherical trees. We also present the concept of splitting maps for the sphere, a key component of this new Spherical Radon Transform, which describes how mass at a point is distributed across the spherical tree. In addition, we examine the orthogonal invariance of splitting maps, which later proves to be a sufficient condition for the injectivity of the Spherical Radon Transform.

3. We propose the novel Spherical Tree-Sliced Wasserstein (STSW) distance for probability distributions on the sphere. By selecting orthogonal invariant splitting maps, we demonstrate that STSW is a invariant metric under orthogonal transformations. Finally, we derive a closed-form [approximation](#) for STSW, enabling an efficient and highly parallelizable implementation.

Organization. The rest of the paper is organized as follows: we review Wasserstein distance variants in §2. We propose the notion of Spherical Trees on the Sphere with a formal construction in §3. We introduce the Spherical Radon Transform on Spherical Trees, and discusses its injectivity in §4. In §5, we propose Spherical Tree-Sliced Wasserstein (STSW) distance and derive a closed-form [approximation](#) for STSW. Finally, we evaluate STSW on various tasks in §6. Theoretical proofs and experimental details are provided in Appendix.

2 PRELIMINARIES

In this section, we review Wasserstein distance, Sliced Wasserstein distance, Wasserstein distance on tree metric spaces and Tree-Sliced Wasserstein distance on Systems of Lines.

Wasserstein Distance. Let Ω be a measurable space, endowed with a metric d , and let μ, ν be two probability distributions on Ω . Denote $\mathcal{P}(\mu, \nu)$ as the set of probability distributions π on the product space $\Omega \times \Omega$ such that $\pi(A \times \Omega) = \mu(A)$ and $\pi(\Omega \times B) = \nu(B)$ for all measurable sets A, B . For $p \geq 1$, the p -Wasserstein distance W_p (Villani, 2008) between μ, ν is defined as:

$$W_p(\mu, \nu) = \inf_{\pi \in \mathcal{P}(\mu, \nu)} \left(\int_{\Omega \times \Omega} d(x, y)^p d\pi(x, y) \right)^{\frac{1}{p}}. \quad (1)$$

Sliced Wasserstein Distance. The Radon Transform (Helgason & Helgason, 2011) is the operator $\mathcal{R} : L^1(\mathbb{R}^d) \rightarrow L^1(\mathbb{R} \times \mathbb{S}^{d-1})$ defined by: for $f \in L^1(\mathbb{R}^d)$, we have $\mathcal{R}f \in L^1(\mathbb{R} \times \mathbb{S}^{d-1})$ such that $\mathcal{R}f(t, \theta) = \int_{\mathbb{R}^d} f(x) \cdot \delta(t - \langle x, \theta \rangle) dx$. Note that \mathcal{R} is a bijection. The Sliced p -Wasserstein

(SW) distance (Bonnel et al., 2015) between $\mu, \nu \in \mathcal{P}(\mathbb{R}^d)$ is defined by:

$$\text{SW}_p(\mu, \nu) := \left(\int_{\mathbb{S}^{d-1}} W_p^p(\mathcal{R}f_\mu(\cdot, \theta), \mathcal{R}f_\nu(\cdot, \theta)) d\sigma(\theta) \right)^{\frac{1}{p}}, \quad (2)$$

where $\sigma = \mathcal{U}(\mathbb{S}^{d-1})$ is the uniform distribution on \mathbb{S}^{d-1} ; and f_μ, f_ν are the probability density functions of μ, ν , respectively.

Tree Wasserstein Distances. Let \mathcal{T} be a rooted tree (as a graph) with non-negative edge lengths, and the ground metric $d_{\mathcal{T}}$, i.e. the length of the unique path between two nodes. Given two probability distributions μ and ν supported on nodes of \mathcal{T} , the Wasserstein distance with ground metric $d_{\mathcal{T}}$, i.e., tree-Wasserstein (TW) (Le et al., 2019), yields a closed-form expression as follows:

$$W_{d_{\mathcal{T}}, 1}(\mu, \nu) = \sum_{e \in \mathcal{T}} w_e \cdot |\mu(\Gamma(v_e)) - \nu(\Gamma(v_e))|, \quad (3)$$

where v_e is the endpoint of edge e that is farther away from the tree root, $\Gamma(v_e)$ is a subtree of \mathbb{T} rooted at v_e , and w_e is the length of e .

Tree-Sliced Wasserstein Distances on Systems of Lines. Tree systems (Tran et al., 2024b) are proposed as replacements of directions in SW. As a topological space, they are constructed by joining (gluing) multiple copies of \mathbb{R} based on a tree (graph) framework, forming a measure metric space in which optimal transport problems admit closed-form solutions. By developing a variant of the Radon Transform that transforms functions on \mathbb{R}^d to functions on tree systems, Tree-Sliced Wasserstein Distances on Systems of Lines (TSW-SL) is introduced in a similar manner as SW. The mentioned closed-form expressions lead to a highly parallelizable implementation for TSW-SL. We next extend the tree systems for measures on a sphere.

3 SPHERICAL TREES ON THE SPHERE

Let d be a positive integer. Recall the notion of the d -dimensional sphere in \mathbb{R}^{d+1} ,

$$\mathbb{S}^d := \{x = (x_0, x_1, \dots, x_d) \in \mathbb{R}^{d+1} : \|x\|_2 = 1\} \subset \mathbb{R}^{d+1}.$$

The sphere \mathbb{S}^d is a complete metric space with metric $d_{\mathbb{S}^d}$ defined as $d_{\mathbb{S}^d}(a, b) = \arccos \langle a, b \rangle_{\mathbb{R}^{d+1}}$ for $a, b \in \mathbb{S}^d$, where $\langle \cdot, \cdot \rangle_{\mathbb{R}^{d+1}}$ is the standard dot product in \mathbb{R}^{d+1} . For $x \in \mathbb{S}^d$, denote H_x be the hyperplane passes through $0 \in \mathbb{R}^{d+1}$ and orthogonal to x , i.e. $H_x = \{y \in \mathbb{R}^{d+1} : \langle x, y \rangle = 0\}$.

We consider the stereographic projection corresponding to x , denoted by φ_x , which is a map from $\mathbb{S}^d \setminus \{x\}$ to H_x defined by: for $y \in \mathbb{S}^d \setminus \{x\}$, $\varphi_x(y)$ is the unique intersection between the line passes through x, y and the hyperplane H_x . In concrete, the formula for φ_x is as follows

$$\begin{aligned} \varphi_x : \quad \mathbb{S}^d \setminus \{x\} &\longrightarrow H_x \\ y &\longmapsto \frac{-\langle x, y \rangle}{1 - \langle x, y \rangle} \cdot x + \frac{1}{1 - \langle x, y \rangle} \cdot y. \end{aligned} \quad (4)$$

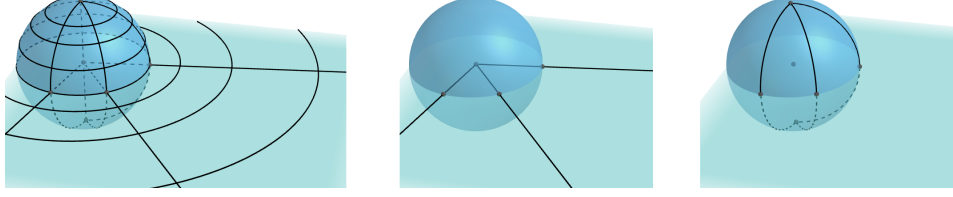
It is well-known that φ_x is a smooth bijection between $\mathbb{S}^d \setminus \{x\}$ and H_x . Moreover, it is convenient to extend φ_x to a map that we also denote by φ_x , from \mathbb{S}^d to $H_x \cup \{\infty\}$, with $\varphi_x(x) = \infty$.

Remark. As a topological space, H_x is homeomorphic to \mathbb{R}^d , and $H_x \cup \{\infty\}$ is the one-point compactification of H_x , which is homeomorphic to \mathbb{S}^d . Also, $H_x \cap \mathbb{S}^d$ is homeomorphic to \mathbb{S}^{d-1} .

Definition 3.1 (Spherical rays in \mathbb{R}^{d+1}). For $y \in \mathbb{S}^d$, ray in \mathbb{R}^{d+1} with direction y is defined as the set $\{t \cdot y : t > 0\} \cup \{\infty\}$. For $x \in \mathbb{S}^d$, and $y \in \mathbb{S}^d \cap H_x$, the spherical ray with root x and direction y , denoted by r_y^x , is defined as the preimage of the ray with direction y through φ_x , i.e., $r_y^x := \varphi_x^{-1}(\{t \cdot y : t > 0\} \cup \{\infty\})$.

An illustration of stereographic projection, rays and spherical rays are presented in Figure 1. In words, a spherical ray with root x and direction y is the great semicircle on surface of the hypersphere passes through y with one endpoint x . We have r_y^x is isometric to the closed interval $[0, \pi]$ via $z \mapsto \arccos \langle x, z \rangle$, and we also have a parameterization of r_y^x as (t, r_y^x) for $0 \leq t \leq \pi$. In particular,

$$\varphi_x^{-1}(0) = -x \mapsto \pi \quad \text{and} \quad \varphi_x^{-1}(\infty) = x \mapsto 0.$$

Figure 1: Illustrations of stereographic projection, rays in \mathbb{R}^3 , and spherical rays in \mathbb{S}^2 .

Let k be a positive integer, $x \in \mathbb{S}^d$ and $y_1, \dots, y_k \in \mathbb{S}^d \cap H_x$ be k distinct points. We have k distinct spherical rays $r_{y_i}^x$ with root x and direction y_i . Consider an equivalence relation \sim on the disjoint union $\bigsqcup_{i=1, \dots, k} r_{y_i}^x$ as follows: For $(t, r_{y_i}^x) \in r_{y_i}^x$ and $(t', r_{y_j}^x) \in r_{y_j}^x$, we have $(t, r_{y_i}^x) \sim (t', r_{y_j}^x)$ if and only if $(t, r_{y_i}^x) = (t', r_{y_j}^x)$ in \mathbb{S}^d . In other words, we identify k point with coordinate 0 on k spherical rays $r_{y_i}^x$. Denote $\mathcal{T}_{y_1, \dots, y_k}^x$ as the set of all equivalence classes in $\bigsqcup_{i=1, \dots, k} r_{y_i}^x$ with respect to the equivalence relation \sim , i.e., $\mathcal{T}_{y_1, \dots, y_k}^x := \left(\bigsqcup_{i=1, \dots, k} r_{y_i}^x \right) / \sim$.

Recall the notion of disjoint union topology and quotient topology in (Hatcher, 2005). For $i = 1, \dots, k$, consider the injection

$$f_i : \quad r_{y_i}^x \hookrightarrow \bigsqcup_{i=1, \dots, k} r_{y_i}^x \\ (t, r_{y_i}^x) \longmapsto (t, r_{y_i}^x).$$

The disjoint union $\bigsqcup_{i=1, \dots, k} r_{y_i}^x$ now becomes a topological space with the disjoint union topology, i.e. the finest topology on $\bigsqcup_{i=1, \dots, k} r_{y_i}^x$ such that the map f_i is continuous for all $i = 1, \dots, k$. Consider the quotient map by the equivalent relation \sim ,

$$\pi : \quad \bigsqcup_{i=1, \dots, k} r_{y_i}^x \longrightarrow \mathcal{T}_{y_1, \dots, y_k}^x = \left(\bigsqcup_{i=1, \dots, k} r_{y_i}^x \right) / \sim \\ (t, r_{y_i}^x) \longmapsto [(t, r_{y_i}^x)].$$

$\mathcal{T}_{y_1, \dots, y_k}^x$ now becomes a topological space with the quotient topology, i.e. the finest topology on $\mathcal{T}_{y_1, \dots, y_k}^x$ such that the map π is continuous. In other words, $\mathcal{T}_{y_1, \dots, y_k}^x$ is formed by gluing k spherical rays $r_{y_i}^x$ at the points with coordinate 0 on each spherical rays.

Definition 3.2 (Spherical Trees in \mathbb{S}^d). The topological space $\mathcal{T}_{y_1, \dots, y_k}^x$ is called a *spherical tree* on \mathbb{S}^d . We said that x is the root and y_1, \dots, y_k are the edges of $\mathcal{T}_{y_1, \dots, y_k}^x$.

A visualization for construction of spherical trees is presented in Figure 2a. The number of edges of a spherical tree is usually denoted by k . For simplicity, we sometimes omit the root x and edges y_1, \dots, y_k and simply denote a spherical tree as \mathcal{T} . The collection of all spherical trees with k edges on \mathbb{S}^d is denoted by \mathbb{T}_k^d . Since $\mathbb{S}^d \cap H_x$ is homeomorphic to the sphere \mathbb{S}^{d-1} , we have the one-to-one correspondence between \mathbb{T}_k^d and the product $\mathbb{S}^d \times (\mathbb{S}^d \cap H_x)^k$ as follows:

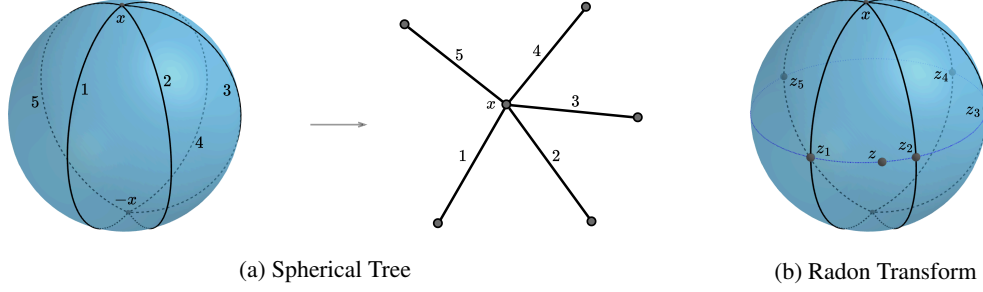
$$\mathcal{T}_{y_1, \dots, y_k}^x \xleftarrow{1-1} x \in \mathbb{S}^d \text{ and } (y_1, \dots, y_k) \in (\mathbb{S}^d \cap H_x)^k \approx (\mathbb{S}^{d-1})^k. \quad (5)$$

From this observation, we can define a *distribution* σ on the space of spherical trees \mathbb{T}_k^d as the joint distribution of distributions on \mathbb{S}^d and \mathbb{S}^{d-1} . For the rest of the paper, let σ be the joint distribution of $(k+1)$ independent distributions, consists of one uniform distributions on \mathbb{S}^d , i.e. $\mathcal{U}(\mathbb{S}^d)$, and k uniform distributions on \mathbb{S}^{d-1} , i.e. $\mathcal{U}(\mathbb{S}^{d-1})$. The topological space \mathcal{T} is metrizable by the metric $d_{\mathcal{T}}$ defined as: For $a = (t, r_{y_i}^x)$ and $b = (t', r_{y_j}^x)$ in \mathcal{T} ,

$$d_{\mathcal{T}}(a, b) = \begin{cases} |t - t'|, & \text{if } i = j, \text{ and} \\ t + t', & \text{if } i \neq j. \end{cases} \quad (6)$$

Moreover, this metric is a tree metric on \mathcal{T} . We verify this by showing for every pair of two points a, b in \mathcal{T} , all paths from a to b in \mathcal{T} are homotopic to each other. Then $d_{\mathcal{T}}(a, b)$ is the length of the shortest path from a to b in \mathcal{T} . Moreover, we can define a measure on \mathcal{T} that induced from the Borel measure on the closed interval $[0, \pi]$. The proof of these properties is similar as the proofs in (Tran et al., 2024b). We summarize our results by a theorem.

216
217
218
219
220
221
222
223
224



225 Figure 2: (a) An illustration of 5 spherical rays with the same root x , along with the corresponding
226 spherical tree rooted at x . Note that, even when endpoints differ from x of these spherical rays
227 are all identical to $-x$ on the sphere, the spherical tree treats these as five distinct points, and only
228 identifies the root x . (b) An illustration of Radon Transform on Spherical Trees. Consider a point z .
229 The hyperplane passing through z and orthogonal to x cuts edges of the spherical tree at 5 points.
230 The mass at z under operator \mathcal{R}^α is distributed across these 5 intersections, depending on α .

231 **Theorem 3.3** (Spherical trees are metric spaces with tree metric). \mathcal{T} is a metric space with tree
232 metric $d_{\mathcal{T}}$. The topology on \mathcal{T} induced by $d_{\mathcal{T}}$ is identical to the topology of \mathcal{T} .
233

234 With this design, in the next section, we will define Lebesgue integrable functions on spherical trees.
235

236 4 SPHERICAL RADON TRANSFORM ON SPHERICAL TREES

237 In this section, we introduce the spherical Radon Transform on Spherical Trees, and discuss the
238 injectivity of our spherical Radon transform variant.
239

240 4.1 A SPHERICAL RADON TRANSFORM VARIANT

241 We introduce the notions of the space of Lebesgue integrable functions on spherical trees. First,
242 denote $L^1(\mathbb{S}^d)$ as the space of Lebesgue integrable functions on \mathbb{S}^d with norm $\|\cdot\|_1$:
243

$$244 L^1(\mathbb{S}^d) = \left\{ f: \mathbb{S}^d \rightarrow \mathbb{R} : \|f\|_1 = \int_{\mathbb{S}^d} |f(x)| dx < \infty \right\}. \quad (7)$$

245 Two functions $f_1, f_2 \in L^1(\mathbb{S}^d)$ are considered to be identical if $f_1(x) = f_2(x)$ for almost every-
246 where on \mathbb{S}^d . Consider a spherical tree \mathcal{T} with root x and k edges y_1, \dots, y_k , a *Lebesgue integrable*
247 *function on \mathcal{T}* is a function $f: \mathcal{T} \rightarrow \mathbb{R}$ such that $\|f\|_{\mathcal{T}} := \sum_{i=1}^k \int_0^\pi |f(t, r_{y_i}^x)| dt < \infty$.
248

249 The *space of Lebesgue integrable functions on \mathcal{T}* is denoted by $L^1(\mathcal{T})$. Two functions $f_1, f_2 \in$
250 $L^1(\mathcal{T})$ are considered to be identical if $f_1(x) = f_2(x)$ for almost everywhere on \mathcal{T} . The space
251 $L^1(\mathcal{L})$ with norm $\|\cdot\|_{\mathcal{T}}$ is a Banach space.
252

253 Let $\Delta_{k-1} := \left\{ (a_i)_{i=1}^k : 0 \leq a_i \leq 1 \text{ and } \sum_{i=1}^k a_i = 1 \right\} \subset \mathbb{R}^k$ be the $(k-1)$ -dimensional standard
254 simplex. Denote $\mathcal{C}(\mathbb{S}^d \times \mathbb{T}_k^d, \Delta_{k-1})$ as the space of continuous maps from $\mathbb{S}^d \times \mathbb{T}_k^d$ to Δ_{k-1} , and
255 called a map in $\mathcal{C}(\mathbb{S}^d \times \mathbb{T}_k^d, \Delta_{k-1})$ by a *splitting map*. Let \mathcal{T} be a spherical tree with root x and k
256 edges y_1, \dots, y_k , α be a splitting map in $\mathcal{C}(\mathbb{S}^d \times \mathbb{T}_k^d, \Delta_{k-1})$, we define an operator associated to α
257 that transforms a Lebesgue integrable functions on \mathbb{S}^d to a Lebesgue integrable functions on \mathcal{T} . For
258 $f \in L^1(\mathbb{S}^d)$, define
259

$$260 \mathcal{R}_{\mathcal{T}}^\alpha f: \mathcal{T} \rightarrow \mathbb{R} \quad (8)$$

$$261 (t, r_{y_i}^x) \mapsto \int_{\mathbb{S}^d} f(y) \cdot \alpha(y, \mathcal{T})_i \cdot \delta(t - \arccos \langle x, y \rangle) dy, \quad (9)$$

262 where δ is the Dirac delta function. We have $\mathcal{R}_{\mathcal{T}}^\alpha f \in L^1(\mathcal{T})$ for $f \in L^1(\mathbb{S}^d)$, and moreover,
263 $\|\mathcal{R}_{\mathcal{T}}^\alpha f\|_{\mathcal{T}} \leq \|f\|_1$. The operator $\mathcal{R}_{\mathcal{T}}^\alpha: L^1(\mathbb{S}^d) \rightarrow L^1(\mathcal{T})$ is a well-defined linear operator. The
264 proof of these properties can be found in Appendix A.1. An illustration of $\mathcal{R}_{\mathcal{T}}^\alpha$ is presented in
265 Figure 2b. We next present a novel spherical Radon Transform variant on spherical trees.
266

Definition 4.1 (Spherical Radon Transform on Spherical Trees). For $\alpha \in \mathcal{C}(\mathbb{S}^d \times \mathbb{T}_k^d, \Delta_{k-1})$, the operator \mathcal{R}^α that is defined as follows:

$$\begin{aligned} \mathcal{R}^\alpha : L^1(\mathbb{S}^d) &\longrightarrow \prod_{\mathcal{T} \in \mathbb{T}_k^d} L^1(\mathcal{T}) \\ f &\longmapsto (\mathcal{R}_{\mathcal{T}}^\alpha f)_{\mathcal{T} \in \mathbb{T}_k^d}. \end{aligned}$$

is called the *Spherical Radon Transform on Spherical Trees*.

4.2 INJECTIVITY OF RADON TRANSFORM ON SPHERICAL TREES

We discuss on the injectivity of our spherical Radon Transform variant. Consider the Euclidean norm on \mathbb{R}^d , i.e. $\|\cdot\|_2$.

Orthogonal group $O(d)$ and its actions. The orthogonal group $O(d)$ is the group of linear transformations of \mathbb{R}^d that preserves the Euclidean norm $\|\cdot\|_2$,

$$O(d) = \{\text{linear transformation } f: \mathbb{R}^d \rightarrow \mathbb{R}^d : \|x\|_2 = \|f(x)\|_2 \text{ for all } x \in \mathbb{R}^d\}. \quad (10)$$

It is well-known that $O(d)$ is isomorphic to the group of orthogonal matrices under multiplication,

$$O(d) = \{Q \in M_{d \times d}(\mathbb{R}) : Q \cdot Q^\top = Q^\top \cdot Q = I_d\}. \quad (11)$$

The canonical group action of $O(d)$ on \mathbb{R}^d is defined by: For $g = Q \in O(d)$ and $y \in \mathbb{R}^d$, we have $y \mapsto gy = Q \cdot y$. By the norm preserving, the action of $O(d+1)$ on \mathbb{R}^{d+1} canonically induces an action of $O(d+1)$ on the sphere \mathbb{S}^d . Moreover, the action of $O(d)$ on \mathbb{R}^d preserves the standard dot product, so the action of $O(d+1)$ on \mathbb{S}^d preserves the metric $d_{\mathbb{S}^d}$.

Group actions of $O(d+1)$ on space of spherical trees \mathbb{T}_k^d . Under $g \in O(d+1)$, the spherical ray r_y^x transforms to r_{gy}^{gx} . It implies that the action of $O(d+1)$ on \mathbb{S}^d canonically induces an action of $O(d+1)$ on \mathbb{T}_k^d as

$$\mathcal{T} = \mathcal{T}_{y_1, \dots, y_k}^x \longmapsto g\mathcal{T} := \mathcal{T}_{gy_1, \dots, gy_k}^{gx}. \quad (12)$$

Moreover, each $g \in O(d+1)$ presents a morphism $\mathcal{T} \rightarrow g\mathcal{T}$ that is isometric.

$O(d+1)$ -invariant splitting maps. Given a map $f: X \rightarrow Y$ and a group G acts on X . The map f is called G -invariant if $f(gx) = f(x)$ for all $g \in G$ and $x \in X$. We have the definition of $O(d+1)$ -invariance in splitting maps.

Definition 4.2. A splitting map α in $\mathcal{C}(\mathbb{S}^d \times \mathbb{T}_k^d, \Delta_{k-1})$ is said to be $O(d+1)$ -invariant, if we have

$$\alpha(gy, g\mathcal{T}) = \alpha(y, \mathcal{T}) \quad (13)$$

for all $(y, \mathcal{T}) \in \mathbb{S}^d \times \mathbb{T}_k^d$ and $g \in O(d+1)$.

With an $O(d+1)$ -invariant splitting maps, our spherical Radon Transform variant is injective.

Theorem 4.3. \mathcal{R}^α is injective for an $O(d+1)$ -invariant splitting map α .

The proof of Theorem 4.3 is presented in Appendix A.3. Finally, we present a candidate for $O(d+1)$ -invariant splitting maps. Define the map $\beta: \mathbb{S}^d \times \mathbb{T}_k^d \rightarrow \mathbb{R}^k$ as follows:

$$\beta(y, \mathcal{T}_{y_1, \dots, y_k}^x)_i = \begin{cases} 0, & \text{if } y = x \text{ or } y = -x, \\ \arccos\left(\frac{\langle y, y_i \rangle}{\sqrt{1 - \langle x, y \rangle^2}}\right) \cdot \sqrt{1 - \langle x, y \rangle^2}, & \text{if } y \neq \pm x. \end{cases} \quad (14)$$

Remark. The construction of β will be explained in Appendix A.2.

The map β is continuous and $O(d+1)$ -invariant. The derivation of β and the proof for these properties are presented in Appendix A.2. We choose $\alpha: \mathbb{S}^d \times \mathbb{T}_k^d \rightarrow \Delta_{k-1}$ as follows:

$$\alpha(y, \mathcal{T}) = \text{softmax}\left(\{\zeta \cdot \beta(y, \mathcal{T})_i\}_{i=1, \dots, k}\right) \quad (15)$$

Here, $\zeta \in \mathbb{R}$ is treated as a tuning parameter. The intuition behind this choice of α is that it reflects the proximity of points to the rays of the spherical trees. As $|\zeta|$ increases, the resulting value of α tends to become more sparse, emphasizing the importance of each ray relative to a specific point.

5 SPHERICAL TREE-SLICED WASSERSTEIN DISTANCE

In this section, we propose our novel Spherical Tree-Sliced Wasserstein Distance (STSW). We also derive a closed-form [approximation](#) of STSW that allows an efficient implementation.

5.1 SPHERICAL TREE-SLICED WASSERSTEIN DISTANCE

Given two probability distributions μ, ν in $\mathcal{P}(\mathbb{S}^d)$, a tree $\mathcal{T} \in \mathbb{T}_k^d$ and an $O(d+1)$ -invariant splitting map $\alpha \in \mathcal{C}(\mathbb{S}^d \times \mathbb{T}_k^d, \Delta_{k-1})$. By the Radon Transform $\mathcal{R}_{\mathcal{T}}^{\alpha}$ in Definition 4.1, μ and ν transform to two probability distributions $\mathcal{R}_{\mathcal{T}}^{\alpha}\mu$ and $\mathcal{R}_{\mathcal{T}}^{\alpha}\nu$ in $\mathcal{P}(\mathcal{T})$. \mathcal{T} is a metric space with tree metric $d_{\mathcal{T}}$ (Tran et al., 2024b), so we can compute Wasserstein distance $W_{d_{\mathcal{T}},1}(\mathcal{R}_{\mathcal{T}}^{\alpha}\mu, \mathcal{R}_{\mathcal{T}}^{\alpha}\nu)$ between $\mathcal{R}_{\mathcal{T}}^{\alpha}\mu$ and $\mathcal{R}_{\mathcal{T}}^{\alpha}\nu$ by Equation (3).

Definition 5.1 (Spherical Tree-Sliced Wasserstein Distance). The *Spherical Tree-Sliced Wasserstein Distance* between μ, ν in $\mathcal{P}(\mathbb{S}^d)$ is defined by:

$$\text{STSW}(\mu, \nu) := \int_{\mathbb{T}_k^d} W_{d_{\mathcal{T}},1}(\mathcal{R}_{\mathcal{T}}^{\alpha}\mu, \mathcal{R}_{\mathcal{T}}^{\alpha}\nu) d\sigma(\mathcal{T}). \quad (16)$$

Remark. Note that, the definition of STSW depends on the space \mathbb{T}_k^d , the distribution σ on \mathbb{T}_k^d , and the splitting map α as in Equation (15). We omit them to simplify the notation.

The STSW distance is, indeed, a metric on $\mathcal{P}(\mathbb{S}^d)$.

Theorem 5.2. *STSW is a metric on $\mathcal{P}(\mathbb{S}^d)$. Moreover, STSW is invariant under orthogonal transformations: For $g \in O(d+1)$, we have*

$$\text{STSW}(\mu, \nu) = \text{STSW}(g\#\mu, g\#\nu), \quad (17)$$

where $g\#\mu, g\#\nu$ as the push-forward of μ, ν via orthogonal transformation $g: \mathbb{S}^d \rightarrow \mathbb{S}^d$, respectively.

The proofs of Theorem 5.2 is presented in Appendix A.4.

5.2 COMPUTATION OF STSW

To approximate the intractable integral in Equation (16), we use the Monte Carlo method as $\widehat{\text{STSW}}(\mu, \nu) = (1/L) \cdot \sum_{l=1}^L W_{d_{\mathcal{T}_l},1}(\mathcal{R}_{\mathcal{T}_l}^{\alpha}\mu, \mathcal{R}_{\mathcal{T}_l}^{\alpha}\nu)$, where $\mathcal{T}_1, \dots, \mathcal{T}_L$ are drawn independently from the distribution σ on \mathbb{T} , and are referred to as projecting tree systems. We present the way to sample \mathcal{T}_i and compute $W_{d_{\mathcal{T}_i},1}(\mathcal{R}_{\mathcal{T}_i}^{\alpha}\mu, \mathcal{R}_{\mathcal{T}_i}^{\alpha}\nu)$.

Sampling spherical trees. Recall that σ is the joint distribution of $k+1$ independent distributions, consists of one uniform distributions on \mathbb{S}^d , and k uniform distributions on \mathbb{S}^{d-1} . This comes from the one-to-one correspondence between \mathbb{T}_k^d and $\mathbb{S}^d \times (\mathbb{S}^{d-1})^k$ as in Equation (5). In applications, to perform a sampling process for $\mathcal{T} = \mathcal{T}_{y_1, \dots, y_k}^x \in \mathbb{T}_k^d$ from σ , we sample by two steps as follows:

1. Sample $k+1$ points x, y_1, \dots, y_k in \mathbb{R}^{d+1} . Normalize them to get x, y_1, \dots, y_k lie on \mathbb{S}^d .
2. For each i , take the intersection of the line passes through x, y_i with H_x , i.e. φ_x , then normalize Φ_x to get new y_i lies on $H_x \cap \mathbb{S}^d$.

This results in a sampling process based on distribution σ .

Computing $W_{d_{\mathcal{T}},1}(\mathcal{R}_{\mathcal{T}}^{\alpha}\mu, \mathcal{R}_{\mathcal{T}}^{\alpha}\nu)$. In applications, given discrete distributions μ and ν as $\mu(x) = \sum_{j=1}^n u_j \cdot \delta(x - a_j)$ and $\nu(x) = \sum_{j=1}^n v_j \cdot \delta(x - a_j)$. We can present μ and ν with the same supports by combining their supports and allow some u_j or v_j to be 0. For spherical tree $\mathcal{T} = \mathcal{T}_{y_1, \dots, y_k}^x$, we want to compute $W_{d_{\mathcal{T}},1}(\mathcal{R}_{\mathcal{T}}^{\alpha}\mu, \mathcal{R}_{\mathcal{T}}^{\alpha}\nu)$. For $1 \leq j \leq n$, let $c_j = d_{\mathbb{S}^d}(x, a_j)$. Also let $c_0 = 0$. By re-indexing, we assume that $0 = c_0 \leq c_1 \leq \dots \leq c_n$. By Radon Transform in Definition 4.1, μ, ν transform to $\mathcal{R}_{\mathcal{T}}^{\alpha}\mu, \mathcal{R}_{\mathcal{T}}^{\alpha}\nu$ supported on $\{(c_j, r_{y_i}^x)\}_{1 \leq i \leq k, 1 \leq j \leq n}$ of \mathcal{T} , with

$$\mathcal{R}_{\mathcal{T}}^{\alpha}\mu(c_j, r_{y_i}^x) = \alpha(a_j, \mathcal{T})_i \cdot u_j \quad \text{and} \quad \mathcal{R}_{\mathcal{T}}^{\alpha}\nu(c_j, r_{y_i}^x) = \alpha(a_j, \mathcal{T})_i \cdot v_j \quad (18)$$

By Equation (3), $W_{d_{\mathcal{T},1}}(\mathcal{R}_{\mathcal{T}}^{\alpha}\mu, \mathcal{R}_{\mathcal{T}}^{\alpha}\nu)$ has a closed-form approximation as follows

$$W_{d_{\mathcal{T},1}}(\mathcal{R}_{\mathcal{T}}^{\alpha}\mu, \mathcal{R}_{\mathcal{T}}^{\alpha}\nu) = \sum_{j=1}^n (c_j - c_{j-1}) \cdot \left(\sum_{i=1}^k \left| \sum_{p=j}^n \alpha(a_p, \mathcal{T})_i \cdot (u_p - v_p) \right| \right). \quad (19)$$

The detailed derivation of Equation (19) is presented in Appendix A.5. The closed-form expression in Equation (19) leads to a highly parallelizable implementation of STSW distance. We summarize our results in this section by Algorithm 1.

Algorithm 1 Spherical Tree-Sliced Wasserstein distance.

Input: $\mu, \nu \in \mathcal{P}(\mathbb{S}^d)$ as $\mu(x) = \sum_{j=1}^n u_j \cdot \delta(x - a_j)$, $\nu(x) = \sum_{j=1}^n v_j \cdot \delta(x - a_j)$, number of spherical trees L , number of rays in spherical trees k , splitting maps α with weight $\delta \in \mathbb{R}$.

for $l = 1$ to L **do**

 Sample $x^{(l)}, y_1^{(l)}, \dots, y_k^{(l)} \stackrel{i.i.d.}{\sim} \mathcal{N}(0, \text{Id}_{d+1})$.

 Compute $x^{(l)} \leftarrow x^{(l)} / \|x^{(l)}\|_2$ and $y_j^{(l)} \leftarrow \varphi_{x^{(l)}}(y_j^{(l)}) / \|\varphi_{x^{(l)}}(y_j^{(l)})\|_2$.

 Construct spherical tree $\mathcal{T}_l = \mathcal{T}_{y_1^{(l)}, \dots, y_k^{(l)}}^{x^{(l)}}$.

 Compute $W_{d_{\mathcal{T}_l,1}}(\mathcal{R}_{\mathcal{T}_l}^{\alpha}\mu, \mathcal{R}_{\mathcal{T}_l}^{\alpha}\nu)$ by Equation (19).

end for

Compute $\widehat{\text{STSW}}(\mu, \nu) = (1/L) \cdot \sum_{l=1}^L W_{d_{\mathcal{T}_l,1}}(\mathcal{R}_{\mathcal{T}_l}^{\alpha}\mu, \mathcal{R}_{\mathcal{T}_l}^{\alpha}\nu)$

Return: $\widehat{\text{STSW}}(\mu, \nu)$.

6 EXPERIMENTAL RESULTS

In this section, we present the results of our four main tasks: Gradient Flow, Self-Supervised Learning, Earth Density Estimation, and Sliced-Wasserstein Auto-Encoder. We provide a detailed evaluation for each task, including quantitative metrics, visualizations, and a comparison with relevant baseline methods. Experimental details can be found in Appendix B.

6.1 GRADIENT FLOW

Our first experiment focuses on learning a target distribution ν from a source distribution μ by minimizing $\text{STSW}(\nu, \mu)$. We solve this optimization using projected gradient descent, as discussed in Bonet et al. (2022). We compare the performance of our method against baselines: SSW (Bonet et al., 2022), and S3W variants (Tran et al., 2024a).

Following Tran et al. (2024a), we use a mixture of 12 von Mises-Fisher distributions (vMFs) as our target ν . The training is conducted over 500 epochs with a full batch size, and each experiment is repeated 10 times. We adopt the evaluation metrics from Tran et al. (2024a), which include log 2-Wasserstein distance, negative log-likelihood (NLL), and training time. As shown in Table 1, STSW outperforms the baselines in all metrics and achieves faster convergence, as illustrated in Figure 10.

6.2 SELF-SUPERVISED LEARNING (SSL)

Normalizing feature vectors to the hypersphere has been shown to improve the quality of learned representations and prevent feature collapse (Chen et al., 2020; Wang & Isola, 2020). In previous work, Wang & Isola (2020) identified two properties of contrastive learning: alignment (bringing positive pairs closer) and uniformity (distributing features evenly on the hypersphere). Adopting the approach in Bonet et al. (2022), we propose replacing the Gaussian kernel uniformity loss with STSW, resulting in the following contrastive objective:

$$\mathcal{L} = \underbrace{\frac{1}{n} \sum_{i=1}^n \|z_i^A - z_i^B\|_2^2}_{\text{Alignment loss}} + \frac{\lambda}{2} \underbrace{(\text{STSW}(z^A, \nu) + \text{STSW}(z^B, \nu))}_{\text{Uniformity loss}}, \quad (20)$$

Table 1: Learning target distribution 12 vFMs. We use $N_R = 30$ rotations for ARI-S3W and an additional learning rate LR = 0.05 for SSW.

Method	$\log W_2 \downarrow$	NLL \downarrow	Runtime(s)
SSW (LR=0.01)	-3.21 ± 0.16	-4980.01 ± 1.89	55.20 ± 0.15
SSW (LR=0.05)	-3.36 ± 0.12	-4976.58 ± 2.23	55.31 ± 0.33
S3W	-2.37 ± 0.21	-4749.67 ± 84.34	1.93 ± 0.06
RI-S3W (1)	-3.12 ± 0.18	-4964.50 ± 27.98	2.03 ± 0.12
RI-S3W (5)	-3.47 ± 0.06	-4984.80 ± 7.32	5.68 ± 0.51
ARI-S3W (30)	-4.39 ± 0.19	-5020.37 ± 6.35	20.25 ± 0.15
STSW	-4.69 ± 0.01	-5041.13 ± 0.84	1.89 ± 0.05

Table 2: CIFAR-10 linear evaluation accuracy for encoded (E) features and projected (P) features on \mathbb{S}^9 , along with pretraining time per epoch. ARI-S3W and RI-S3W use 5 rotations.

Method	Acc. E(%) \uparrow	Acc. P(%) \uparrow	Time (s/ep.)
Hypersphere	79.81	74.64	10.18
SimCLR	79.97	72.80	9.34
SW	74.39	67.80	9.65
SSW	70.23	64.33	10.59
S3W	78.59	73.83	10.14
RI-S3W (5)	79.93	73.95	10.22
ARI-S3W (5)	80.08	75.12	10.19
STSW	80.53	76.78	<u>9.54</u>

where $\nu = \mathcal{U}(\mathbb{S}^d)$, $\lambda > 0$ is regularization factor, $z^A, z^B \in \mathbb{R}^{n \times (d+1)}$ are embeddings of two image augmentations mapped onto \mathbb{S}^d . Similar to Bonet et al. (2022) and Tran et al. (2024a), we train ResNet18 (He et al., 2016) based encoder on the CIFAR-10 (Krizhevsky et al., 2009) w.r.t \mathcal{L} . After this, we train a linear classifier on the features extracted from the pre-trained encoder.

Table 2 demonstrates the improvement of STSW in comparison to baselines: Hypersphere (Wang & Isola, 2020), SimCLR (Chen et al., 2020), SW, SSW, and S3W variants. We also conduct experiments with $d = 2$ to visualize learned representations. Figure 12 illustrates that STSW can effectively distribute encoded features around the sphere while keeping similar ones close together.

6.3 EARTH DENSITY ESTIMATION

We now demonstrate the application of STSW in density estimation on \mathbb{S}^2 . Data used in this task is collected by (Mathieu & Nickel, 2020) which consists of Fire (Brakenridge, 2017), Earthquake (EOSDIS, 2020) and Flood (EOSDIS, 2020). As in (Bonet et al., 2022), we employ an exponential map normalizing flow model (Rezende et al., 2020) which are invertible transformations T and aim to minimize $\min_T \text{STSW}(T_{\#}\mu, p_Z)$, where μ is the empirical distribution, and p_Z is a prior distribution on \mathbb{S}^2 which we use uniform distribution. The density for any point $x \in \mathbb{S}^2$ is then estimated by $f_{\mu}(x) = p_Z(T(x))|\det J_T(x)|$ where $J_T(x)$ is the Jacobian of T at x .

Our baselines are exponential map normalizing flows with SW, SSW, and S3W variants, and stereographic projection-based (Dinh et al., 2016) normalizing flows. As seen in Table 3, STSW even with fewer epochs and shorter training time (10K epochs over 2h10m for STSW versus 20K epochs over 4h30m for ARI-S3W, both on Fire dataset) still outperforms or is competitive with SSW and S3W variants.

6.4 SLICED-WASSERSTEIN AUTO-ENCODER (SWAE)

We apply STSW to generative modeling using the Sliced-Wasserstein Auto-Encoder (SWAE) (Kolouri et al., 2018) framework, which regularizes the latent space distribution to match a prior

Table 3: Negative log-likelihood on test data, averaged over 5 runs with different data split.

Method	Quake ↓	Flood ↓	Fire ↓
Stereo	1.94 ± 0.21	1.92 ± 0.04	1.31 ± 0.12
SW	0.99 ± 0.05	1.47 ± 0.03	0.55 ± 0.21
SSW	0.84 ± 0.06	1.26 ± 0.04	0.23 ± 0.20
S3W	0.89 ± 0.08	1.35 ± 0.04	0.34 ± 0.05
RI-S3W (1)	0.80 ± 0.07	1.25 ± 0.03	0.14 ± 0.06
ARI-S3W (50)	0.77 ± 0.06	1.24 ± 0.03	0.08 ± 0.05
STSW	0.68 ± 0.04	1.23 ± 0.03	-0.67 ± 0.05

Table 4: SWAE results evaluated on latent regularization of CIFAR-10 test data.

Method	log W_2 ↓	NLL ↓	BCE ↓	Time (s/ep.)
SW	-3.2943	-0.0014	0.6314	3.4060
SSW	-2.2234	0.0005	0.6309	8.2386
S3W	-3.3421	0.0013	0.6329	4.5138
RI-S3W (5)	-3.1950	-0.0039	0.6354	4.9682
ARI-S3W (5)	-3.3935	0.0012	0.6330	4.7347
STSW	-3.4191	-0.0051	0.6341	<u>3.5460</u>

distribution q . Let $\varphi : \mathcal{X} \rightarrow \mathbb{S}^d$ and $\psi : \mathbb{S}^d \rightarrow \mathcal{X}$ be the parametric encoder and decoder. The objective of the SWAE is:

$$\min_{\varphi, \psi} \mathbb{E}_{x \sim p} [c(x, \psi(\varphi(x)))] + \lambda \cdot \text{STSW}(\varphi_{\#} p, q) \quad (21)$$

where λ controls regularization, p is data distribution. We use SW, SSW (Bonet et al., 2022) and S3W variants (Tran et al., 2024a) as baselines, Binary Cross Entropy (BCE) for reconstruction loss and a mixture of 10 vMFs as the prior, similar to Tran et al. (2024a). We provide results in Table 4. We note that STSW has the best results in log 2-Wasserstein and NLL with a competitive training time, though its BCE slightly underperforms the others.

7 CONCLUSION

This paper introduces the Spherical Tree-Sliced Wasserstein (STSW) distance, a novel approach leveraging a new integration domain called spherical trees. In contrast to the traditional one-dimensional lines or great semicircles often used in the spherical Sliced Wasserstein variant, STSW utilizes spherical trees to better capture the topology of spherical data and provides closed-form solutions for optimal transport problems on spherical trees, leading to expected improvements in both performance and efficiency. We rigorously develop the theoretical basis for our approach by introducing spherical Radon Transform on Spherical Tree then verifying the core properties of the transform such as its injectivity. We thoroughly develop the theoretical foundation for this method by introducing the spherical Radon Transform on Spherical Trees and validating its key properties, such as injectivity. STSW is derived from the Radon Transform framework, and through careful construction of the splitting maps, we obtain a closed-form approximation for the distance. Through empirical tasks on spherical data, we demonstrate that STSW significantly outperforms recent spherical Wasserstein variants. Future research could explore spherical trees further, such as developing sampling processes for spherical trees or adapting Generalized Radon Transforms to enhance STSW.

540 **Ethics Statement.** Given the nature of the work, we do not foresee any negative societal and ethical
541 impacts of our work.

542 **Reproducibility Statement.** Source codes for our experiments are provided in the supplementary
543 materials of the paper. The details of our experimental settings and computational infrastructure are
544 given in Section 6 and the Appendix. All datasets that we used in the paper are published, and they
545 are easy to access in the Internet.
546

547 REFERENCES

- 548 Clément Bonet, Paul Berg, Nicolas Courty, François Septier, Lucas Drumetz, and Minh-Tan Pham.
549 Spherical sliced-wasserstein. *arXiv preprint arXiv:2206.08780*, 2022.
550
- 551 Nicolas Bonneel, Julien Rabin, Gabriel Peyré, and Hanspeter Pfister. Sliced and radon wasserstein
552 barycenters of measures. *Journal of Mathematical Imaging and Vision*, 51:22–45, 2015.
553
- 554 G. Brakenridge. Global active archive of large flood events. [http://floodobservatory.
555 colorado.edu/Archives/index.html](http://floodobservatory.colorado.edu/Archives/index.html), 2017.
556
- 557 Paolo Cabella and Domenico Marinucci. Statistical challenges in the analysis of cosmic microwave
558 background radiation. 2009.
- 559 Mathilde Caron, Ishan Misra, Julien Mairal, Priya Goyal, Piotr Bojanowski, and Armand Joulin.
560 Unsupervised learning of visual features by contrasting cluster assignments. *Advances in neural
561 information processing systems*, 33:9912–9924, 2020.
562
- 563 Ting Chen, Simon Kornblith, Mohammad Norouzi, and Geoffrey Hinton. A simple framework for
564 contrastive learning of visual representations. In *International conference on machine learning*,
565 pp. 1597–1607. PMLR, 2020.
- 566 Benjamin Coors, Alexandru Paul Condurache, and Andreas Geiger. Spherenet: Learning spherical
567 representations for detection and classification in omnidirectional images. In *Proceedings of the
568 European conference on computer vision (ECCV)*, pp. 518–533, 2018.
- 569 Li Cui, Xin Qi, Chengfeng Wen, Na Lei, Xinyuan Li, Min Zhang, and Xianfeng Gu. Spherical
570 optimal transportation. *Computer-Aided Design*, 115:181–193, 2019.
571
- 572 Marco Cuturi. Sinkhorn distances: Lightspeed computation of optimal transport. *Advances in neural
573 information processing systems*, 26, 2013.
- 574 Tim R Davidson, Luca Falorsi, Nicola De Cao, Thomas Kipf, and Jakub M Tomczak. Hyperspheri-
575 cal variational auto-encoders. *arXiv preprint arXiv:1804.00891*, 2018.
576
- 577 Marco Di Marzio, Agnese Panzera, and Charles C Taylor. Nonparametric regression for spherical
578 data. *Journal of the American Statistical Association*, 109(506):748–763, 2014.
- 579 Laurent Dinh, Jascha Sohl-Dickstein, and Samy Bengio. Density estimation using real nvp. *arXiv
580 preprint arXiv:1605.08803*, 2016.
581
- 582 Ayelet Dunitz and Allen Tannenbaum. Texture mapping via optimal mass transport. *IEEE trans-
583 actions on visualization and computer graphics*, 16(3):419–433, 2009.
- 584 Asi Elad, Yosi Keller, and Ron Kimmel. Texture mapping via spherical multi-dimensional scaling.
585 In *Scale Space and PDE Methods in Computer Vision: 5th International Conference, Scale-Space
586 2005, Hofgeismar, Germany, April 7-9, 2005. Proceedings 5*, pp. 443–455. Springer, 2005.
587
- 588 EOSDIS. Active fire data. [https://earthdata.nasa.gov/
589 earth-observation-data/near-real-time/firms/active-fire-data](https://earthdata.nasa.gov/earth-observation-data/near-real-time/firms/active-fire-data),
590 2020. Land, Atmosphere Near real-time Capability for EOS (LANCE) system operated by
591 NASA’s Earth Science Data and Information System (ESDIS).
- 592 Kilian Fatras, Younes Zine, Rémi Flamary, Rémi Gribonval, and Nicolas Courty. Learning with
593 minibatch wasserstein: asymptotic and gradient properties. *arXiv preprint arXiv:1910.04091*,
2019.

- 594 Charles Fefferman, Sanjoy Mitter, and Hariharan Narayanan. Testing the manifold hypothesis.
595 *Journal of the American Mathematical Society*, 29(4):983–1049, 2016.
596
- 597 Jean-Bastien Grill, Florian Strub, Florent Altché, Corentin Tallec, Pierre Richemond, Elena
598 Buchatskaya, Carl Doersch, Bernardo Avila Pires, Zhaohan Guo, Mohammad Gheshlaghi Azar,
599 et al. Bootstrap your own latent—a new approach to self-supervised learning. *Advances in neural
600 information processing systems*, 33:21271–21284, 2020.
- 601 Brittany Froese Hamfeldt and Axel GR Turnquist. A convergence framework for optimal transport
602 on the sphere. *Numerische Mathematik*, 151(3):627–657, 2022.
603
- 604 Allen Hatcher. *Algebraic topology*. 2005.
- 605 Kaiming He, Xiangyu Zhang, Shaoqing Ren, and Jian Sun. Deep residual learning for image recog-
606 nition. In *Proceedings of the IEEE conference on computer vision and pattern recognition*, pp.
607 770–778, 2016.
608
- 609 Sigurdur Helgason and Sigurdur Helgason. The radon transform on \mathbb{R}^n . *Integral Geometry and
610 Radon Transforms*, pp. 1–62, 2011.
611
- 612 SR Jammalamadaka. *Topics in Circular Statistics*, volume 336. World Scientific, 2001.
- 613 San Jiang, Kan You, Yaxin Li, Duojie Weng, and Wu Chen. 3d reconstruction of spherical images:
614 a review of techniques, applications, and prospects. *Geo-spatial Information Science*, pp. 1–30,
615 2024.
616
- 617 PE Jupp. Some applications of directional statistics to astronomy. *New trends in probability and
618 statistics*, 3:123–133, 1995.
- 619 Renata Khasanova and Pascal Frossard. Graph-based classification of omnidirectional images. In
620 *Proceedings of the IEEE International Conference on Computer Vision Workshops*, pp. 869–878,
621 2017.
622
- 623 D Kinga, Jimmy Ba Adam, et al. A method for stochastic optimization. In *International conference
624 on learning representations (ICLR)*, volume 5, pp. 6. San Diego, California;, 2015.
- 625 Soheil Kolouri, Phillip E Pope, Charles E Martin, and Gustavo K Rohde. Sliced wasserstein auto-
626 encoders. In *International Conference on Learning Representations*, 2018.
627
- 628 Alex Krizhevsky. Learning multiple layers of features from tiny images. 2009. URL <https://api.semanticscholar.org/CorpusID:18268744>.
629
- 630 Alex Krizhevsky, Geoffrey Hinton, et al. Learning multiple layers of features from tiny images.
631 2009.
632
- 633 Tam Le, Makoto Yamada, Kenji Fukumizu, and Marco Cuturi. Tree-sliced variants of wasserstein
634 distances. *Advances in neural information processing systems*, 32, 2019.
635
- 636 Christophe Ley and Thomas Verdebout. *Modern directional statistics*. Chapman and Hall/CRC,
637 2017.
- 638 Weiyang Liu, Yandong Wen, Zhiding Yu, Ming Li, Bhiksha Raj, and Le Song. Sphereface: Deep
639 hypersphere embedding for face recognition. In *Proceedings of the IEEE conference on computer
640 vision and pattern recognition*, pp. 212–220, 2017.
641
- 642 Kanti V Mardia and Peter E Jupp. *Directional statistics*. John Wiley & Sons, 2009.
- 643 Emile Mathieu and Maximilian Nickel. Riemannian continuous normalizing flows. *Advances in
644 Neural Information Processing Systems*, 33:2503–2515, 2020.
645
- 646 Nathanaël Perraudin, Michaël Defferrard, Tomasz Kacprzak, and Raphael Sgier. DeepSphere: Effi-
647 cient spherical convolutional neural network with healpix sampling for cosmological applications.
Astronomy and Computing, 27:130–146, 2019.

- 648 Arthur Pewsey and Eduardo García-Portugués. Recent advances in directional statistics. *Test*, 30
649 (1):1–58, 2021.
- 650 Gabriel Peyré, Marco Cuturi, et al. Computational optimal transport: With applications to data
651 science. *Foundations and Trends® in Machine Learning*, 11(5-6):355–607, 2019.
- 652 Michael Quellmalz, Robert Beinert, and Gabriele Steidl. Sliced optimal transport on the sphere.
653 *Inverse Problems*, 39(10):105005, 2023.
- 654 Julien Rabin, Gabriel Peyré, Julie Delon, and Marc Bernot. Wasserstein barycenter and its applica-
655 tion to texture mixing. In *International Conference on Scale Space and Variational Methods in*
656 *Computer Vision*, pp. 435–446, 2011.
- 657 Danilo Jimenez Rezende, George Papamakarios, Sébastien Racaniere, Michael Albergo, Gurtej
658 Kanwar, Phiala Shanahan, and Kyle Cranmer. Normalizing flows on tori and spheres. In *In-*
659 *ternational Conference on Machine Learning*, pp. 8083–8092. PMLR, 2020.
- 660 Meyer Scetbon, Marco Cuturi, and Gabriel Peyré. Low-rank Sinkhorn factorization. *International*
661 *Conference on Machine Learning (ICML)*, 2021.
- 662 Huy Tran, Yikun Bai, Abihith Kothapalli, Ashkan Shahbazi, Xinran Liu, Rocio P Diaz Martin, and
663 Soheil Kolouri. Stereographic spherical sliced wasserstein distances. In *Forty-first International*
664 *Conference on Machine Learning*, 2024a.
- 665 Viet-Hoang Tran, Trang Pham, Tho Tran, Tam Le, and Tan M Nguyen. Tree-sliced wasserstein
666 distance on a system of lines. *arXiv preprint arXiv:2406.13725*, 2024b.
- 667 C. Villani. *Optimal Transport: Old and New*, volume 338. Springer Science & Business Media,
668 2008.
- 669 Jiri Vrba and Stephen E Robinson. Signal processing in magnetoencephalography. *Methods*, 25(2):
670 249–271, 2001.
- 671 Tongzhou Wang and Phillip Isola. Understanding contrastive representation learning through align-
672 ment and uniformity on the hypersphere. In *International conference on machine learning*, pp.
673 9929–9939. PMLR, 2020.
- 674 Zhirong Wu, Yuanjun Xiong, Stella X Yu, and Dahua Lin. Unsupervised feature learning via non-
675 parametric instance discrimination. In *Proceedings of the IEEE conference on computer vision*
676 *and pattern recognition*, pp. 3733–3742, 2018.
- 677 Jiacheng Xu and Greg Durrett. Spherical latent spaces for stable variational autoencoders. *arXiv*
678 *preprint arXiv:1808.10805*, 2018.
- 679 Mingxuan Yi and Song Liu. Sliced wasserstein variational inference. In *Asian Conference on*
680 *Machine Learning*, pp. 1213–1228. PMLR, 2023.
- 681
682
683
684
685
686
687
688
689
690
691
692
693
694
695
696
697
698
699
700
701

702	NOTATION	
703		
704		
705	\mathbb{R}^d	d -dimensional Euclidean space
706	$\ \cdot\ _2$	Euclidean norm
707	$\langle \cdot, \cdot \rangle$	standard dot product
708	\mathbb{S}^d	d -dimensional hypersphere
709	θ	unit vector
710	\sqcup	disjoint union
711	\arccos	inverse of cosine function
712	$L^1(X)$	space of Lebesgue integrable functions on X
713	$\mathcal{P}(X)$	space of probability distributions on X
714	μ, ν	measures
715	$\delta(\cdot)$	1-dimensional Dirac delta function
716	$\mathcal{U}(\mathbb{S}^d)$	uniform distribution on \mathbb{S}^d
717	$\#$	pushforward (measure)
718	$\mathcal{C}(X, Y)$	space of continuous maps from X to Y
720	$d(\cdot, \cdot)$	metric in metric space
721	$O(d)$	orthogonal group of order d
722	g	element of group
723	W_p	p -Wasserstein distance
724	SW_p	Sliced p -Wasserstein distance
725	Γ	(rooted) subtree
726	e	edge in graph
727	w_e	weight of edge in graph
728	φ_x	stereographic projection at x
729	H_x	hyperplane passes through x and orthogonal to x
730	r_y^x	spherical ray
731	$\mathcal{T}, \mathcal{T}_{y_1, \dots, y_k}^x$	spherical tree
732	\mathbb{T}_k^d	space of spherical trees of k edges on \mathbb{S}^d
733	σ	distribution on space of tree systems
734	L	number of spherical tree
735	k	number of edges in spherical tree
736	\mathcal{R}	original Radon Transform
737	\mathcal{R}^α	spherical Radon Transform on Spherical Trees
738	Δ_{k-1}	$(k - 1)$ -dimensional standard simplex
739	α	splitting map
740	ζ	tuning parameter in splitting maps
741		
742		
743		
744		
745		
746		
747		
748		
749		
750		
751		
752		
753		
754		
755		

Supplement to “Spherical Tree-Sliced Wasserstein Distance”

Table of Contents

A	Theoretical Proofs	15
A.1	Properties of $\mathcal{R}_T^\alpha f$	15
A.2	Derivation and properties of splitting maps	16
A.3	Proof of Theorem 4.3	17
A.4	Proof of Theorem 5.2	21
A.5	Derivation for the closed-form approximation of STSW	22
B	Experimental details	23
B.1	Evolution of STSW	23
B.2	Runtime Analysis	25
B.3	Gradient Flow	26
B.4	Self-Supervised Learning	27
B.5	Earth Data Estimation	28
B.6	Generative Models	28

A THEORETICAL PROOFS

A.1 PROPERTIES OF $\mathcal{R}_T^\alpha f$

Proof. Let $f \in L^1(\mathbb{S}^d)$. We show that $\|\mathcal{R}_T^\alpha f\|_{\mathcal{T}} \leq \|f\|_1$. Note that, $\arccos \langle x, y \rangle \in [0, \pi]$, so we have

$$\begin{aligned}
 \|\mathcal{R}_T^\alpha f\|_{\mathcal{T}} &= \sum_{i=1}^k \int_0^\pi |\mathcal{R}_T^\alpha f(t, r_{y_i}^x)| dt \\
 &= \sum_{i=1}^k \int_0^\pi \left| \int_{\mathbb{S}^d} f(y) \cdot \alpha(y, \mathcal{T})_i \cdot \delta(t - \arccos \langle x, y \rangle) dy \right| dt \\
 &\leq \sum_{i=1}^k \int_0^\pi \left(\int_{\mathbb{S}^d} |f(y)| \cdot \alpha(y, \mathcal{T})_i \cdot \delta(t - \arccos \langle x, y \rangle) dy \right) dt \\
 &= \sum_{i=1}^k \int_{\mathbb{S}^d} \left(\int_0^\pi |f(y)| \cdot \alpha(y, \mathcal{T})_i \cdot \delta(t - \arccos \langle x, y \rangle) dt \right) dy \\
 &= \sum_{i=1}^k \int_{\mathbb{S}^d} |f(y)| \cdot \alpha(y, \mathcal{T})_i \cdot \left(\int_0^\pi \delta(t - \arccos \langle x, y \rangle) dt \right) dy \\
 &= \sum_{i=1}^k \int_{\mathbb{S}^d} |f(y)| \cdot \alpha(y, \mathcal{T})_i dy \\
 &= \int_{\mathbb{S}^d} |f(y)| \cdot \left(\sum_{i=1}^k \alpha(y, \mathcal{T})_i \right) dy \\
 &= \int_{\mathbb{S}^d} |f(y)| dy
 \end{aligned}$$

$$= \|f\|_1 < \infty.$$

It implies that $\mathcal{R}_{\mathcal{T}}^{\alpha} f \in L^1(\mathcal{T})$, which means the operator $\mathcal{R}_{\mathcal{T}}^{\alpha}: L^1(\mathbb{S}^d) \rightarrow L^1(\mathcal{T})$ is well-defined. Clearly, $\mathcal{R}_{\mathcal{T}}^{\alpha}$ is a linear operator. \square

A.2 DERIVATION AND PROPERTIES OF SPLITTING MAPS

We recall the construction for a splitting map α presented in Subsection 4.2. We have a map $\beta: \mathbb{S}^d \times \mathbb{T}_k^d \rightarrow \mathbb{R}^k$ defined as follows:

$$\beta(y, \mathcal{T}_{y_1, \dots, y_k}^x)_i = \begin{cases} 0, & \text{if } y = x \text{ or } y = -x, \text{ and} \\ \arccos\left(\frac{\langle y, y_i \rangle}{\sqrt{1 - \langle x, y \rangle^2}}\right) \cdot \sqrt{1 - \langle x, y \rangle^2}, & \text{if } y \neq x, -x. \end{cases} \quad (22)$$

Then $\alpha: \mathbb{S}^d \times \mathbb{T}_k^d \rightarrow \Delta_{k-1}$ is defined as follows:

$$\alpha(y, \mathcal{T}) = \text{softmax}\left(\{\delta \cdot \beta(y, \mathcal{T})_i\}_{i=1, \dots, k}\right) \quad (23)$$

We will show that

1. Where does β come from?
2. α is continuous.
3. α is $O(d+1)$ -invariant.

Proof. We prove each part.

1. For $(y, \mathcal{T}_{y_1, \dots, y_k}^x) \in \mathbb{S}^d \times \mathbb{T}_k^d$, let N_y be the hyperplane passes through Y and orthogonal to x . Then N_y intersects the spherical ray $r_{y_i}^x$ at a single point a , and intersects the vector x at a single point b . The $\beta(y, \mathcal{T})_i$ is the length of the small arc from y to a on the circle centered at b passes through y and a . Indeed, if $y = x$ and $y = -x$, this length is equal to 0, the same as the definition of β . If $y \neq x, -x$, let c is the intersection of the line passes through x, y , and the hyperplane H_x ; moreover, let d be the unique intersection of the segment with endpoints $0, c$, and the hyperplane H_x . In details, we have

$$c = \varphi_x(y) \text{ and } d = \frac{c}{\|c\|_2}. \quad (24)$$

Note that, the condition $y \neq x, -x$ is to guarantee that $c \neq 0, \infty$. We compute c in details as follows:

$$c = \frac{-\langle x, y \rangle}{1 - \langle x, y \rangle} \cdot x + \frac{1}{1 - \langle x, y \rangle} \cdot y, \quad (25)$$

so

$$d = \frac{c}{\|c\|_2} = \frac{\frac{-\langle x, y \rangle}{1 - \langle x, y \rangle} \cdot x + \frac{1}{1 - \langle x, y \rangle} \cdot y}{\left\| \frac{-\langle x, y \rangle}{1 - \langle x, y \rangle} \cdot x + \frac{1}{1 - \langle x, y \rangle} \cdot y \right\|_2} \quad (26)$$

$$= \frac{\frac{-\langle x, y \rangle}{1 - \langle x, y \rangle} \cdot x + \frac{1}{1 - \langle x, y \rangle} \cdot y}{\sqrt{\left\langle \frac{-\langle x, y \rangle}{1 - \langle x, y \rangle} \cdot x + \frac{1}{1 - \langle x, y \rangle} \cdot y \right\rangle}} \quad (27)$$

$$= \frac{\frac{-\langle x, y \rangle}{1 - \langle x, y \rangle} \cdot x + \frac{1}{1 - \langle x, y \rangle} \cdot y}{\sqrt{\|x\|_2^2 \cdot \frac{\langle x, y \rangle^2}{(1 - \langle x, y \rangle)^2} + \|y\|_2^2 \cdot \frac{1}{(1 - \langle x, y \rangle)^2} - 2 \cdot \langle x, y \rangle \cdot \frac{\langle x, y \rangle}{(1 - \langle x, y \rangle)^2}}} \quad (28)$$

$$\begin{aligned}
&= \frac{-\langle x, y \rangle}{1 - \langle x, y \rangle} \cdot x + \frac{1}{1 - \langle x, y \rangle} \cdot y \\
&= \frac{-\langle x, y \rangle \cdot x + y}{\sqrt{\frac{1 - \langle x, y \rangle^2}{(1 - \langle x, y \rangle)^2}}}
\end{aligned} \tag{29}$$

$$= \frac{-\langle x, y \rangle \cdot x + y}{\sqrt{1 - \langle x, y \rangle^2}}. \tag{30}$$

Note that, since b is the projection of y on vector x , so we have

$$b = \langle x, y \rangle \cdot x. \tag{31}$$

By similarity, we have

$$\frac{\text{length of arc from } y \text{ to } a \text{ on the circle centered at } b \text{ passes through } y \text{ and } a}{\text{length of arc from } d \text{ to } y_i \text{ on the circle centered at } 0 \text{ passes through } d \text{ and } y_i} = \frac{\|y - b\|_2}{\|d - 0\|_2}. \tag{32}$$

Note that, the length of arc from d to y_i on the circle centered at 0 passes through d and y_i is

$$d_{\mathbb{S}^d}(d, y_i) = \arccos \langle d, y_i \rangle, \tag{33}$$

so

$$\text{length of arc from } y \text{ to } a \text{ on the circle centered at } b \text{ passes through } y \text{ and } a \tag{34}$$

$$= \arccos \langle d, y_i \rangle \cdot \frac{\|y - b\|_2}{\|d - 0\|_2} \tag{35}$$

$$= \arccos \langle d, y_i \rangle \cdot \|y - b\|_2 \tag{36}$$

$$= \arccos \left\langle \frac{-\langle x, y \rangle \cdot x + y}{\sqrt{1 - \langle x, y \rangle^2}}, y_i \right\rangle \cdot \|y - \langle x, y \rangle \cdot x\|_2 \tag{37}$$

$$= \arccos \left(\frac{\langle y, y_i \rangle}{\sqrt{1 - \langle x, y \rangle^2}} \right) \cdot \sqrt{\|y\|_2^2 + \langle x, y \rangle^2 \cdot \|x\|_2^2 - 2 \langle x, y \rangle \cdot \langle x, y \rangle} \tag{38}$$

$$= \arccos \left(\frac{\langle y, y_i \rangle}{\sqrt{1 - \langle x, y \rangle^2}} \right) \cdot \sqrt{1 - \langle x, y \rangle^2} \tag{39}$$

$$= \beta(y, \mathcal{T}_{y_1, \dots, y_k}^x)_i. \tag{40}$$

We finish the derivation of β . In context of splitting maps, this is a reasonable choice, since it relates to evaluate distances from a point to a spherical ray.

2. The derivation of β clearly implies that β is continuous. We can also check the continuous of β directly from the formula of β . Since β is continuous, we have α is continuous.

3. We have β is $O(d + 1)$ -invariant since orthogonal transformations preserve the standard dot product. Since β is $O(d + 1)$ -invariant, we have α is $O(d + 1)$ -invariant. \square

A.3 PROOF OF THEOREM 4.3

Proof. Recall the notion of (vertical) Radon Transform (Quellmalz et al., 2023). Let Φ^d be the collection of all spherical rays on \mathbb{S}^d , i.e.

$$\Phi^d := \{r_y^x : x \in \mathbb{S}^d, y \in H_x\}. \tag{41}$$

Note that, this is the same as the collection of all spherical trees with one edge, i.e. \mathbb{T}_1^d . For $f \in L^1(\mathbb{S}^d)$, consider the map $(\mathcal{R}r_y^x)f : r_y^x \equiv [0, \pi] \rightarrow \mathbb{R}$ defined by

$$(\mathcal{R}r_y^x)f(t) = \int_{\mathbb{S}^d} f(z) \cdot \delta(t - \arccos \langle z, x \rangle) dz. \tag{42}$$

Similar to Appendix A.1, we can show that $(\mathcal{R}r_y^x)f \in L^1(r_y^x)$. We have an operator

$$\mathcal{R} : L^1(\mathbb{S}^d) \longrightarrow \bigsqcup_{r_y^x \in \Phi^d} L^1(r_y^x) \quad (43)$$

$$f \longmapsto \left((\mathcal{R}r_y^x)f \right)_{r_y^x \in \Phi^d} \quad (44)$$

This is exactly the (vertical) Radon Transform for Lebesgue integrable functions on \mathbb{S}^d , as in (Quellmalz et al., 2023). This is proved to be an injective linear operator, so if $(\mathcal{R}r_y^x)f = 0$ for all $r_y^x \in \Phi^d$, then $f = 0$.

Back to the problem. Recall that \mathbb{T}_k^d is the space of all spherical trees of k edges on \mathbb{S}^d ,

$$\mathbb{T}_k^d = \{ \mathcal{T}_{y_1, \dots, y_k}^x = (r_{y_1}^x, \dots, r_{y_k}^x) : x \in \mathbb{S}^d \text{ and } y_1, \dots, y_k \in H_x \}. \quad (45)$$

For an $1 \leq i \leq k$ and $r_y^x \in \Phi^d$, define

$$\mathbb{T}_k^d(i, r_y^x) := \{ \mathcal{T}_{y_1, \dots, y_k}^x : y = y_i \}. \quad (46)$$

In words, $\mathbb{T}_k^d(i, r_y^x)$ is a subcollection of \mathbb{T}_k^d consists of all spherical trees with root x and the i^{th} spherical ray is $r_{y_i}^x$. It is clear that \mathbb{T}_k^d is the disjoint union of all $\mathbb{T}_k^d(i, r_y^x)$ for $r_y^x \in \Phi^d$,

$$\mathbb{T}_k^d = \bigsqcup_{r_y^x \in \Phi^d} \mathbb{T}_k^d(i, r_y^x). \quad (47)$$

We have some observations on subcollections $\mathbb{T}_k^d(i, r_y^x)$.

Result 1. Each orthogonal transformation $g \in O(d+1)$ define a bijection between $\mathbb{T}_k^d(i, r_y^x)$ and $\mathbb{T}_k^d(i, r_{gy}^{gx})$. In details, the map ϕ_g defined by

$$\phi_g : \mathbb{T}_k^d(i, r_y^x) \longrightarrow \mathbb{T}_k^d(i, r_{gy}^{gx}) \quad (48)$$

$$\mathcal{T}_{y_1, \dots, y_k}^x \longmapsto \mathcal{T}_{gy_1, \dots, gy_k}^{gx}. \quad (49)$$

is a well-defined and is a bijection. This can be verified directly by definitions.

Result 2. For $1 \leq i \leq k$ and $r_y^x, r_{y'}^{x'} \in \Phi^d$, we have

$$\int_{\mathbb{T}_k^d(i, r_y^x)} \alpha(z, \mathcal{T})_i d\mathcal{T} = \int_{\mathbb{T}_k^d(i, r_{y'}^{x'})} \alpha(z', \mathcal{T})_i d\mathcal{T} \quad (50)$$

for all $z, z' \in \mathbb{S}^d$ such that $d_{\mathbb{S}^d}(x, z) = d_{\mathbb{S}^d}(x', z')$. Note that, the intergrations are taken over a $\mathbb{T}_k^d(i, r_y^x)$ and $\mathbb{T}_k^d(i, r_{y'}^{x'})$ with measures induced from the measure of \mathbb{L}_k^d . To prove Equation (50), we first show it in two specific cases as follows:

- Case 1. Assume $x = x'$ and $y = y'$.
- Case 2. Assume z lies on r_y^x and z' lies on $r_{y'}^{x'}$.

If we can show that Equation (50) holds for assumptions in case 1 and 2, then Equation (50) holds for all x, y, z, x', y', z' . Indeed, assume that Equation (50) holds for assumptions in case 1 and 2. Then for all x, y, z, x', y', z' , we consider $t \in r_y^x$ and $t' \in r_{y'}^{x'}$ such that

$$d_{\mathbb{S}^d}(x, t) = d_{\mathbb{S}^d}(x, z) = d_{\mathbb{S}^d}(x', z') = d_{\mathbb{S}^d}(x', t'). \quad (51)$$

Then from the results in case 1 and 2, we have

972
973
974
975
976
977
978
979
980
981
982
983
984
985
986
987
988
989
990
991
992
993
994
995
996
997
998
999
1000
1001
1002
1003
1004
1005
1006
1007
1008
1009
1010
1011
1012
1013
1014
1015
1016
1017
1018
1019
1020
1021
1022
1023
1024
1025

$$\int_{\mathbb{T}_k^d(i, r_y^x)} \alpha(z, \mathcal{T})_i d\mathcal{T} \stackrel{\text{by case 1}}{=} \int_{\mathbb{T}_k^d(i, r_y^x)} \alpha(t, \mathcal{T})_i d\mathcal{T} \quad (52)$$

$$\stackrel{\text{by case 2}}{=} \int_{\mathbb{T}_k^d(i, r_{y'}^x)} \alpha(t', \mathcal{T})_i d\mathcal{T} \stackrel{\text{by case 1}}{=} \int_{\mathbb{T}_k^d(i, r_{y'}^x)} \alpha(z', \mathcal{T})_i d\mathcal{T}. \quad (53)$$

So Equation (50) holds for all x, y, z, x', y', z' . Now we prove it holds for case 1 and 2.

For case 1, from the transitivity of orthogonal transformations on \mathbb{S}^d , there exists $g \in O(d+1)$ such that

$$gx = x, gy = y, gz = z'. \quad (54)$$

From **Result 1**, there is a corresponding bijection ϕ_g from $\mathbb{T}_k^d(i, r_y^x)$ to $\mathbb{T}_k^d(i, r_{y'}^x)$. We have

$$\int_{\mathbb{T}_k^d(i, r_{y'}^x)} \alpha(z', \mathcal{T})_i d\mathcal{T} = \int_{\mathbb{T}_k^d(i, r_y^x)} \alpha(z', g\mathcal{T})_i d(g\mathcal{T}) \quad (\text{change of variables}) \quad (55)$$

$$= \int_{\mathbb{T}_k^d(i, r_y^x)} \alpha(gz, g\mathcal{T})_i d(g\mathcal{T}) \quad (\text{since } z' = gz) \quad (56)$$

$$= \int_{\mathbb{T}_k^d(i, r_y^x)} \alpha(z, \mathcal{T})_i d(g\mathcal{T}) \quad (\text{since } \alpha \text{ is } O(d+1)\text{-invariant}) \quad (57)$$

$$= \int_{\mathbb{T}_k^d(i, r_y^x)} \alpha(z, \mathcal{T})_i d(\mathcal{T}) \quad (\text{since } |\det(g)| = 1) \quad (58)$$

$$(59)$$

So Equation (50) holds for case 1. A similar proof can be processed for case 2. From the transitivity of orthogonal transformations on \mathbb{S}^d , there exists $h \in O(d+1)$ such that

$$hx = x', hy = y', hz = z'. \quad (60)$$

From **Result 1**, there is a corresponding bijection ϕ_h from $\mathbb{T}_k^d(i, r_y^x)$ to $\mathbb{T}_k^d(i, r_{y'}^{x'})$. We have

$$\int_{\mathbb{T}_k^d(i, r_{y'}^{x'})} \alpha(z', \mathcal{T})_i d\mathcal{T} = \int_{\mathbb{T}_k^d(i, r_y^x)} \alpha(z', h\mathcal{T})_i d(h\mathcal{T}) \quad (\text{change of variables}) \quad (61)$$

$$= \int_{\mathbb{T}_k^d(i, r_y^x)} \alpha(hz, h\mathcal{T})_i d(h\mathcal{T}) \quad (\text{since } z' = hz) \quad (62)$$

$$= \int_{\mathbb{T}_k^d(i, r_y^x)} \alpha(z, \mathcal{T})_i d(h\mathcal{T}) \quad (\text{since } \alpha \text{ is } O(d+1)\text{-invariant}) \quad (63)$$

$$= \int_{\mathbb{T}_k^d(i, r_y^x)} \alpha(z, \mathcal{T})_i d(\mathcal{T}) \quad (\text{since } |\det(h)| = 1) \quad (64)$$

$$(65)$$

We finish the proof for **Result 2**.

Result 3. From **Result 2**, for all $1 \leq i \leq k$ and $t \in [0, \pi]$, we can define a constant $c_i(t)$ such that

$$c_i(t) := \int_{\mathbb{T}_k^d(i, r_y^x)} \alpha(z, \mathcal{T})_i d\mathcal{T} \quad (66)$$

for all $r_y^x \in \Phi^d$ and $z \in \mathbb{S}^d$ such that $t = d_{\mathbb{S}^d}(x, z) = \arccos \langle x, z \rangle$. Then for all $t \in [0, \pi]$, we have

$$c_1(t) + c_2(t) + \dots + c_k(t) = 1. \quad (67)$$

To show this, first, denote $\mathbb{T}_k^d(x)$ as the collection of all spherical trees with root x on \mathbb{S}^d . We have

$$\mathbb{T}_k^d(x) = \bigsqcup_{y \in H_x \cap \mathbb{S}^d} \mathbb{T}_k^d(i, r_y^x), \quad (68)$$

1026 so we have

$$1027 \int_{\mathbb{T}_k^d(x)} \alpha(z, \mathcal{T})_i d\mathcal{T} = \int_{H_x \cap \mathbb{S}^d} \left(\int_{\mathbb{T}_k^d(i, r_y^x)} \alpha(z, \mathcal{T})_i d\mathcal{T} \right) dy \quad (69)$$

$$1029 = \int_{H_x \cap \mathbb{S}^d} c_i(\arccos \langle x, z \rangle) dy \quad (70)$$

$$1031 = c_i(\arccos \langle x, z \rangle). \quad (71)$$

1032 Then

$$1033 c_1(\arccos \langle x, z \rangle) + \dots + c_k(\arccos \langle x, z \rangle) = \sum_{i=1}^k \int_{\mathbb{T}_k^d(x)} \alpha(z, \mathcal{T})_i d\mathcal{T} \quad (72)$$

$$1035 = \int_{\mathbb{T}_k^d(x)} \left(\sum_{i=1}^k \alpha(z, \mathcal{T})_i \right) d\mathcal{T} \quad (73)$$

$$1037 = \int_{\mathbb{T}_k^d(x)} 1 d\mathcal{T} \quad (74)$$

$$1039 = 1. \quad (75)$$

1040 We finish the proof for **Result 3**.

1041 Consider a splitting map α in $\mathcal{C}(\mathbb{S}^d \times \mathbb{T}_k^d, \Delta_{k-1})$ that is $O(d+1)$ -invariant. For a function $f \in L^1(\mathbb{S}^d)$, for each $1 \leq i \leq k$, define a function $g_i \in L^1([0, \pi] \times \Phi^d)$ as follows

$$1042 g_i : [0, \pi] \times \Phi^d \longrightarrow \mathbb{R} \quad (76)$$

$$1043 (t, r_y^x) \longmapsto \int_{\mathbb{T}_k^d(i, r_y^x)} \mathcal{R}_{\mathcal{T}}^\alpha f(t, r_y^x) d\mathcal{T}. \quad (77)$$

1044 From the definition of $\mathcal{R}_{\mathcal{T}}^\alpha f$,

$$1045 \mathcal{R}_{\mathcal{T}}^\alpha f : \mathcal{T} \longrightarrow \mathbb{R} \quad (78)$$

$$1046 (t, r_{y_i}^x) \longmapsto \int_{\mathbb{S}^d} f(y) \cdot \alpha(y, \mathcal{T})_i \cdot \delta(t - \arccos \langle x, y \rangle) dy, \quad (79)$$

1047 we have

$$1048 g_i(t, r_y^x) = \int_{\mathbb{T}_k^d(i, r_y^x)} \mathcal{R}_{\mathcal{T}}^\alpha f(t, r_y^x) d\mathcal{T} \quad (80)$$

$$1050 = \int_{\mathbb{T}_k^d(i, r_y^x)} \left(\int_{\mathbb{S}^d} f(z) \cdot \alpha(z, \mathcal{T})_i \cdot \delta(t - \arccos \langle x, z \rangle) dz \right) d\mathcal{T} \quad (81)$$

$$1052 = \int_{\mathbb{S}^d} \left(\int_{\mathbb{T}_k^d(i, r_y^x)} f(z) \cdot \alpha(z, \mathcal{T})_i \cdot \delta(t - \arccos \langle x, z \rangle) d\mathcal{T} \right) dz \quad (82)$$

$$1054 = \int_{\mathbb{S}^d} f(z) \cdot \delta(t - \arccos \langle x, z \rangle) \cdot \left(\int_{\mathbb{T}_k^d(i, r_y^x)} \alpha(z, \mathcal{T})_i d\mathcal{T} \right) dz \quad (83)$$

$$1056 = \int_{\mathbb{S}^d} f(z) \cdot \delta(t - \arccos \langle x, z \rangle) \cdot c_i(\arccos \langle x, z \rangle) dz \quad (84)$$

$$1058 = c_i(t) \cdot \int_{\mathbb{S}^d} f(z) \cdot \delta(t - \arccos \langle x, z \rangle) dz \quad (85)$$

$$1060 = c_i(t) \cdot (\mathcal{R}r_y^x) f(t). \quad (86)$$

1061 So

$$1062 \sum_{i=1}^k g_i(t, r_y^x) = \sum_{i=1}^k c_i(t) \cdot (\mathcal{R}r_y^x) f(t) \quad (87)$$

$$= \left(\sum_{i=1}^k c_i(t) \right) \cdot (\mathcal{R}r_y^x) f(t) = 1 \cdot (\mathcal{R}r_y^x) f(t) = (\mathcal{R}r_y^x) f(t) \quad (88)$$

Let $f \in \text{Ker } \mathcal{R}^\alpha$, which means $\mathcal{R}_T^\alpha f = 0$ for all $T \in \mathbb{T}_k^d$. So $g = 0 \in L^1([0, \pi] \times \Phi^d)$ for all $1 \leq i \leq k$. It implies $(\mathcal{R}r_y^x) f = 0 \in L^1(r_y^x)$ for all $r_y^x \in \Phi^d$. So, from the (vertical) Radon Transform is injective, we conclude that $f = 0 \in L^1(\mathbb{S}^d)$. so \mathcal{R}^α is injective. \square

Remark. To formalize the proof above, the notion of Haar measure for compact groups is required. However, we simplify the explanation as it goes beyond the scope of this paper.

A.4 PROOF OF THEOREM 5.2

Proof. We want to show that

$$\text{STSW}(\mu, \nu) = \int_{\mathbb{T}_k^d} \mathbf{W}_{d_T, 1}(\mathcal{R}_T^\alpha \mu, \mathcal{R}_T^\alpha \nu) d\sigma(T). \quad (89)$$

is a metric on $\mathcal{P}(\mathbb{S}^d)$.

Positive definiteness. For $\mu, \nu \in \mathcal{P}(\mathbb{S}^d)$, it is clear that $\text{STSW}(\mu, \mu) = 0$ and $\text{STSW}(\mu, \nu) \geq 0$. If $\text{STSW}(\mu, \nu) = 0$, then $\mathbf{W}_{d_T, 1}(\mathcal{R}_T^\alpha \mu, \mathcal{R}_T^\alpha \nu) = 0$ for all $T \in \mathbb{T}_k^d$. Since $\mathbf{W}_{d_T, 1}$ is a metric on $\mathcal{P}(T)$, we have $\mathcal{R}_T^\alpha \mu = \mathcal{R}_T^\alpha \nu$ for all $T \in \mathbb{T}_k^d$. By the injectivity of our Radon transform variant, we have $\mu = \nu$.

Symmetry. For $\mu, \nu \in \mathcal{P}(\mathbb{S}^d)$, we have:

$$\text{STSW}(\mu, \nu) = \int_{\mathbb{T}_k^d} \mathbf{W}_{d_T, 1}(\mathcal{R}_T^\alpha \mu, \mathcal{R}_T^\alpha \nu) d\sigma(T) \quad (90)$$

$$= \int_{\mathbb{T}_k^d} \mathbf{W}_{d_T, 1}(\mathcal{R}_T^\alpha \nu, \mathcal{R}_T^\alpha \mu) d\sigma(T) = \text{STSW}(\nu, \mu). \quad (91)$$

So $\text{STSW}(\mu, \nu) = \text{STSW}(\nu, \mu)$.

Triangle inequality. For $\mu_1, \mu_2, \mu_3 \in \mathcal{P}(\mathbb{S}^d)$, we have:

$$\text{STSW}(\mu_1, \mu_2) + \text{STSW}(\mu_2, \mu_3) \quad (92)$$

$$= \int_{\mathbb{T}_k^d} \mathbf{W}_{d_T, 1}(\mathcal{R}_T^\alpha \mu_1, \mathcal{R}_T^\alpha \mu_2) d\sigma(T) + \int_{\mathbb{T}_k^d} \mathbf{W}_{d_T, 1}(\mathcal{R}_T^\alpha \mu_2, \mathcal{R}_T^\alpha \mu_3) d\sigma(T) \quad (93)$$

$$= \int_{\mathbb{T}_k^d} \left(\mathbf{W}_{d_T, 1}(\mathcal{R}_T^\alpha \mu_1, \mathcal{R}_T^\alpha \mu_2) + \mathbf{W}_{d_T, 1}(\mathcal{R}_T^\alpha \mu_2, \mathcal{R}_T^\alpha \mu_3) \right) d\sigma(T) \quad (94)$$

$$\geq \int_{\mathbb{T}_k^d} \mathbf{W}_{d_T, 1}(\mathcal{R}_T^\alpha \mu_1, \mathcal{R}_T^\alpha \mu_3) d\sigma(T) \quad (95)$$

$$= \text{STSW}(\mu_1, \mu_3). \quad (96)$$

So the triangle inequality holds for STSW.

We conclude that STSW is a metric on the space $\mathcal{P}(\mathbb{S}^d)$.

$O(d+1)$ -invariance of STSW. For $g \in O(d+1)$, we show that

$$\text{STSW}(\mu, \nu) = \text{STSW}(g\#\mu, g\#\nu), \quad (97)$$

where $g\#\mu, g\#\nu$ as the pushforward of μ, ν via orthogonal transformation $g: \mathbb{S}^d \rightarrow \mathbb{S}^d$, respectively. For $T = \mathcal{T}_{y_1, \dots, y_k}^x \in \mathbb{T}_k^d$, we have $gT = \mathcal{T}_{gy_1, \dots, gy_k}^{gx}$. Note that $|\det(g)| = 1$, so

$$\mathcal{R}_{gT}^\alpha(g\#\mu)(t, r_{gy_i}^{gx}) = \int_{\mathbb{S}^d} g\#\mu(y) \cdot \alpha(y, gT)_i \cdot \delta(t - \arccos \langle gx, y \rangle) dy \quad (98)$$

$$= \int_{\mathbb{S}^d} \mu(g^{-1}y) \cdot \alpha(y, g\mathcal{T})_i \cdot \delta(t - \arccos \langle gx, y \rangle) dy \quad (99)$$

$$= \int_{\mathbb{S}^d} \mu(g^{-1}gy) \cdot \alpha(gy, g\mathcal{T})_i \cdot \delta(t - \arccos \langle gx, gy \rangle) d(gy) \quad (100)$$

$$= \int_{\mathbb{S}^d} \mu(y) \cdot \alpha(y, \mathcal{T})_i \cdot \delta(t - \arccos \langle x, y \rangle) d(y) \quad (101)$$

$$= \mathcal{R}_{\mathcal{T}}^{\alpha} \mu(t, r_{y_i}^x). \quad (102)$$

Similarly, we have

$$\mathcal{R}_{g\mathcal{T}}^{\alpha}(g\sharp\nu)(t, r_{gy_i}^{gx}) = \mathcal{R}_{\mathcal{T}}^{\alpha}\nu(t, r_{y_i}^x). \quad (103)$$

Since g induces an isometric transformation $\mathcal{T} \rightarrow g\mathcal{T}$, so

$$\mathbb{W}_{d_{\mathcal{T}},1}(\mathcal{R}_{\mathcal{T}}^{\alpha}\mu, \mathcal{R}_{\mathcal{T}}^{\alpha}\nu) = \mathbb{W}_{d_{g\mathcal{T}},1}(\mathcal{R}_{g\mathcal{T}}^{\alpha}g\sharp\mu, \mathcal{R}_{g\mathcal{T}}^{\alpha}g\sharp\nu). \quad (104)$$

We have

$$\text{STSW}(g\sharp\mu, g\sharp\nu) = \int_{\mathbb{T}_k^d} \mathbb{W}_{d_{\mathcal{T}},1}(\mathcal{R}_{\mathcal{T}}^{\alpha}g\sharp\mu, \mathcal{R}_{\mathcal{T}}^{\alpha}g\sharp\nu) d\sigma(\mathcal{T}) \quad (105)$$

$$= \int_{\mathbb{T}_k^d} \mathbb{W}_{d_{g\mathcal{T}},1}(\mathcal{R}_{g\mathcal{T}}^{\alpha}g\sharp\mu, \mathcal{R}_{g\mathcal{T}}^{\alpha}g\sharp\nu) d\sigma(g\mathcal{T}) \quad (106)$$

$$= \int_{\mathbb{T}_k^d} \mathbb{W}_{d_{\mathcal{T}},1}(\mathcal{R}_{\mathcal{T}}^{\alpha}\mu, \mathcal{R}_{\mathcal{T}}^{\alpha}\nu) d\sigma(\mathcal{T}) \quad (107)$$

$$= \text{STSW}(\mu, \nu) \quad (108)$$

So STSW is $O(d+1)$ -invariant. \square

A.5 DERIVATION FOR THE CLOSED-FORM APPROXIMATION OF STSW

We derive the closed-form [approximation](#) of STSW for two discrete probability distributions μ and ν given as follows

$$\mu(x) = \sum_{j=1}^n u_j \cdot \delta(x - a_j) \quad \text{and} \quad \nu(x) = \sum_{i=j}^n v_j \cdot \delta(x - a_j). \quad (109)$$

We can write μ and ν in these forms by combining their supports and allow some u_j and v_j to be 0. Consider spherical tree $\mathcal{T} = \mathcal{T}_{y_1, \dots, y_k}^x$. For $1 \leq j \leq n$, let $c_j = d_{\mathbb{S}^d}(x, a_j)$, and also let $c_0 = 0$. By re-indexing, we assume that the sequence c_0, \dots, c_n is increasing,

$$0 = c_0 \leq c_1 \leq c_2 \leq \dots \leq c_n. \quad (110)$$

For $0 \leq j \leq n$ and $1 \leq i \leq k$, consider all points $x_j^{(i)} = (c_j, r_{y_i}^x)$ on the spherical tree \mathcal{T} . Since $c_0 = 0$, we have

$$x_0^{(1)} = x_0^{(2)} = \dots = x_0^{(k)} = x, \quad (111)$$

and for $1 \leq j \leq n$, $x_j^{(i)}$ is exactly the unique intersection between the hyperplane passes through a_j and orthogonal to x , and the spherical ray $r_{y_i}^x$. We compute $\mathcal{R}_{\mathcal{T}}^{\alpha}\mu$: For $t \in [0, \pi]$ and $1 \leq i \leq k$,

$$\mathcal{R}_{\mathcal{T}}^{\alpha}\mu(t, r_{y_i}^x) = \int_{\mathbb{S}^d} \mu(y) \cdot \alpha(y, \mathcal{T})_i \cdot \delta(t - \arccos \langle x, y \rangle) dy \quad (112)$$

$$= \int_{\mathbb{S}^d} \left(\sum_{j=1}^n u_j \cdot \delta(y - a_j) \right) \cdot \alpha(y, \mathcal{T})_i \cdot \delta(t - \arccos \langle x, y \rangle) dy \quad (113)$$

$$= \sum_{j=1}^n u_j \cdot \int_{\mathbb{S}^d} \alpha(y, \mathcal{T})_i \cdot (\delta(y - a_j) \cdot \delta(t - \arccos \langle x, y \rangle)) dy. \quad (114)$$

So,

- 1188 1. If $t \notin \{c_1, \dots, c_n\}$, then $\mathcal{R}_{\mathcal{T}}^{\alpha}\mu(t, r_{y_i}^x) = 0$; and,
 1189
 1190 2. If $t = c_j$ for some j , then $\mathcal{R}_{\mathcal{T}}^{\alpha}\mu(t, r_{y_i}^x) = \mathcal{R}_{\mathcal{T}}^{\alpha}\mu(c_j, r_{y_i}^x) = \mathcal{R}_{\mathcal{T}}^{\alpha}\mu(x_j^{(i)}) = \alpha(a_j, \mathcal{T})_i \cdot u_j$.

1191 Similarly, we have

- 1193 1. If $t \notin \{c_1, \dots, c_n\}$, then $\mathcal{R}_{\mathcal{T}}^{\alpha}\nu(t, r_{y_i}^x) = 0$; and,
 1194
 1195 2. If $t = c_j$ for some j , then $\mathcal{R}_{\mathcal{T}}^{\alpha}\nu(t, r_{y_i}^x) = \mathcal{R}_{\mathcal{T}}^{\alpha}\nu(c_j, r_{y_i}^x) = \mathcal{R}_{\mathcal{T}}^{\alpha}\nu(x_j^{(i)}) = \alpha(a_j, \mathcal{T})_i \cdot v_j$.

1196 For $1 \leq j \leq n$ and $1 \leq i \leq k$, let

$$1197 u_j^{(i)} = \alpha(a_j, \mathcal{T})_i \cdot u_j \quad \text{and} \quad v_j^{(i)} = \alpha(a_j, \mathcal{T})_i \cdot v_j. \quad (115)$$

1199 Consider \mathcal{T} as a graph with nodes $x_j^{(i)}$ for $1 \leq i \leq k, 0 \leq j \leq n$. Note that $x_0^{(i)} = x$ for all i , and
 1200 we assign this is the root of \mathcal{T} . Two nodes is adjacent is the shortest path on \mathcal{T} does not contain any
 1201 other nodes. In other words, the set of edges in \mathcal{T} are $e_j^{(i)} = (x_j^{(i)}, x_{j-1}^{(i)})$ for $1 \leq i \leq k, 1 \leq j \leq n$,
 1202 and $e_j^{(i)} = (x_j^{(i)}, x_{j-1}^{(i)})$ has length $c_j - c_{j-1}$. For an edge $e_j^{(i)}$, its further endpoint from the root
 1203 is $x_j^{(i)}$. Also, for a node $x_j^{(i)}$ with $j > 0$, the corresponding subtree $\Gamma(x_j^{(i)})$ contains all nodes
 1204 $x_p^{(i)}$ with $j \leq p \leq n$. From these above observations, we can see μ and ν transform to $\mathcal{R}_{\mathcal{T}}^{\alpha}\mu$ and
 1205 $\mathcal{R}_{\mathcal{T}}^{\alpha}\nu$ supported on nodes of \mathcal{T} , where the mass at node $x_j^{(i)}$ is $u_j^{(i)}$ and $v_j^{(i)}$, respectively. So, from
 1206 Equation (3), we have

$$1207 W_{d_{\mathcal{T}}, 1}(\mathcal{R}_{\mathcal{T}}^{\alpha}\mu, \mathcal{R}_{\mathcal{T}}^{\alpha}\nu) = \sum_{e \in \mathcal{T}} w_e \cdot |\mu(\Gamma(v_e)) - \nu(\Gamma(v_e))| \quad (116)$$

$$1210 = \sum_{i=1}^k \sum_{j=1}^n (c_j - c_{j-1}) \cdot |\mu(\Gamma(x_j^{(i)})) - \nu(\Gamma(x_j^{(i)}))| \quad (117)$$

$$1214 = \sum_{j=1}^n (c_j - c_{j-1}) \cdot \left(\sum_{i=1}^k |\mu(\Gamma(x_j^{(i)})) - \nu(\Gamma(x_j^{(i)}))| \right) \quad (118)$$

$$1215 = \sum_{j=1}^n (c_j - c_{j-1}) \cdot \left(\sum_{i=1}^k \left| \sum_{p=j}^n \mu(x_p^{(i)}) - \sum_{p=j}^n \nu(x_p^{(i)}) \right| \right) \quad (119)$$

$$1217 = \sum_{j=1}^n (c_j - c_{j-1}) \cdot \left(\sum_{i=1}^k \left| \sum_{p=j}^n u_p^{(i)} - \sum_{p=j}^n v_p^{(i)} \right| \right) \quad (120)$$

$$1222 = \sum_{j=1}^n (c_j - c_{j-1}) \cdot \left(\sum_{i=1}^k \left| \sum_{p=j}^n (u_p^{(i)} - v_p^{(i)}) \right| \right) \quad (121)$$

$$1225 = \sum_{j=1}^n (c_j - c_{j-1}) \cdot \left(\sum_{i=1}^k \left| \sum_{p=j}^n \alpha(a_p, \mathcal{T})_i \cdot (u_p - v_p) \right| \right) \quad (122)$$

$$1230 \quad (123)$$

1231 This is identical to Equation (19). We finish the derivation.

1232 B EXPERIMENTAL DETAILS

1233 All our experiments were conducted on a single NVIDIA H100 80G GPU. For all tasks, if not
 1234 specified, hyperparameter ζ in STSW is set to its default value of 2.

1235 B.1 EVOLUTION OF STSW

1236 In this section, we examine the evolution of STSW as well as different distances when measuring
 1237 two distributions. In line with (Bonet et al., 2022; Tran et al., 2024a), we select source distribution
 1238

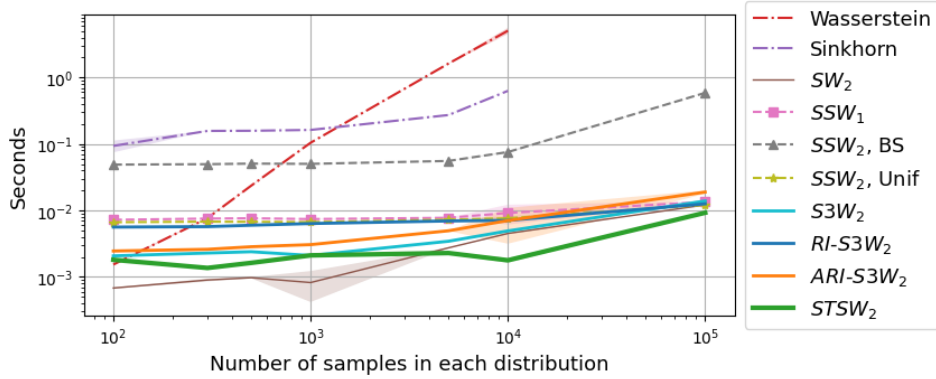


Figure 3: Runtime Comparison, averaged over 15 runs. We set $L = 200$ for all methods. For our STSW, we use 200 trees and 10 lines. The computation time of STSW includes the generation of the tree system.

$\text{vMF}(\cdot, 0)$ a.k.a uniform distribution and target distribution $\text{vMF}(\mu, \kappa)$. We initialize 500 samples in each distribution. We use $\kappa = 10$, $L = 200$ trees, $k = 10$ lines for STSW, $L = 200$ projections for other sliced metrics, $N_R = 100$ rotations for RI-S3W, ARI-S3W, and a pool size of 1000 for ARI-S3W in all experiments unless specified otherwise. Results are averaged over 20 runs.

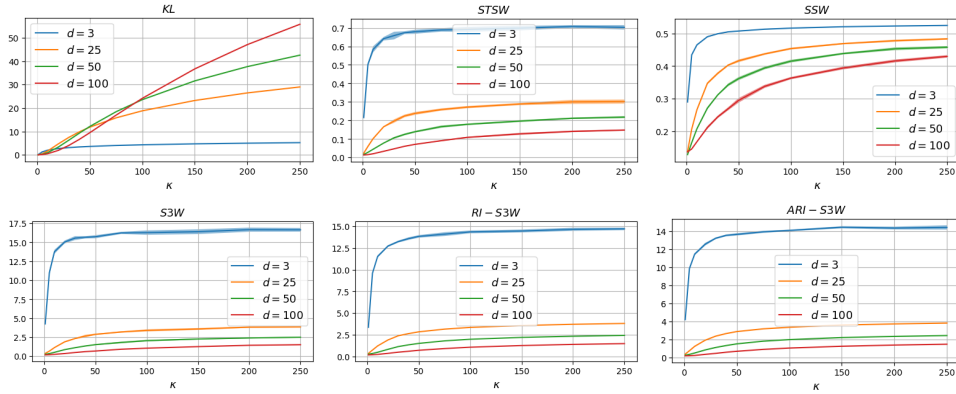


Figure 4: Evolution between $\text{vMF}(\mu, \kappa)$ and $\text{vMF}(\cdot, 0)$ w.r.t κ on \mathbb{S}^{d-1} across various methods. We use $\kappa \in \{1, 5, 10, 20, 30, 40, 50, 75, 100, 150, 200, 250\}$

Evolution w.r.t κ . Figure 4 shows the evolution of various methods w.r.t to κ . As expected, STSW aligns with the trends in S3W and SSW, decreasing with higher dimensions, unlike KL divergence. Here, we use a derived form for KL divergence (Davidson et al., 2018; Xu & Durrett, 2018) as follows:

$$\begin{aligned} \text{KL}(\text{vMF}(\mu, \kappa) \parallel \text{vMF}(\cdot, 0)) &= \kappa \frac{I_{(d+1)/2}(\kappa)}{I_{(d+1)/2-1}(\kappa)} + \left(\frac{d+1}{2} - 1 \right) \log \kappa - \frac{d+1}{2} \log(2\pi) \\ &\quad - \log I_{(d+1)/2-1}(\kappa) + \frac{d+1}{2} \log \pi + \log 2 - \log \Gamma \left(\frac{d+1}{2} \right). \end{aligned}$$

Evolution w.r.t rotated vMFs. Next, we evaluate a fixed vMF distribution and its rotation along a great circle. Specifically, we compute metric between $\text{vMF}((1, 0, 0, \dots), \kappa)$ and $\text{vMF}((\cos \theta, \sin \theta, 0, \dots), \kappa)$ for $\theta \in \{(k\pi)/6\}_{k=0}^{12}$. We plot results in Figure 5

1296
1297
1298
1299
1300
1301
1302
1303
1304
1305
1306
1307
1308
1309
1310
1311
1312
1313
1314
1315
1316
1317
1318
1319
1320
1321
1322
1323
1324
1325
1326
1327
1328
1329
1330
1331
1332
1333
1334
1335
1336
1337
1338
1339
1340
1341
1342
1343
1344
1345
1346
1347
1348
1349

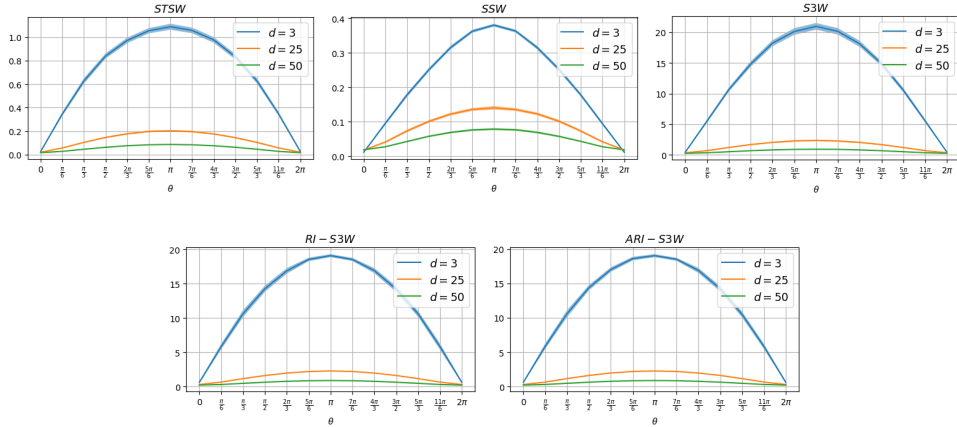


Figure 5: Evolution between rotated vMFs distributions, averaged over 100 runs. d denotes data dimension.

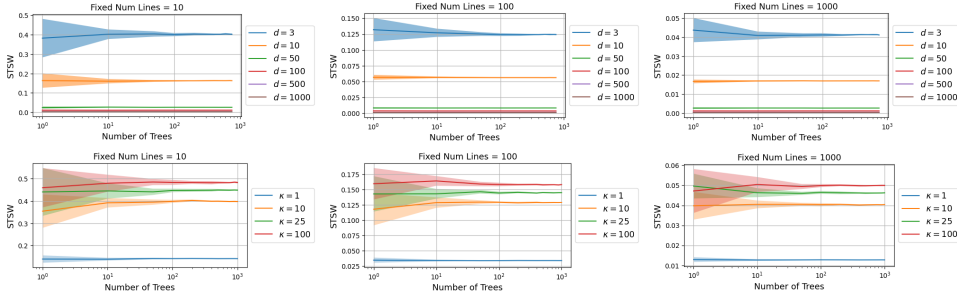


Figure 6: Evolution of STSW between the source and target distributions when varying number of trees $L \in \{1, 10, 50, 100, 200, 400, 500, 750, 900, 1000\}$.

Evolution of STSW w.r.t Number of Trees, Number of Lines and ζ . Next, we study the effect of the number of trees and lines on STSW. If not specified, we fix $\kappa = 10$ and $d = 3$. We present the results in Figure 6, Figure 7, and Figure 8

B.2 RUNTIME ANALYSIS

Runtime Comparison. We now perform a runtime comparison with other commonly used distance metrics, including the traditional Wasserstein, Sinkhorn (Cuturi, 2013), Sliced-Wasserstein (SW), Spherical Sliced-Wasserstein (SSW) (Bonet et al., 2022) as well as Stereographic Spherical Sliced Wasserstein (S3W) (Tran et al., 2024a) and its variants (RI-S3W, ARI-S3W). For a fair comparison, we also include SSW_2 with binary search (BS) and Unif when a closed form is available for uniform distribution. The runtime of applying each of these methods on two distribution on S^2 is illustrated in Figure 3. We highlight that STSW offers a significant improvement in computational efficiency over other metrics.

Runtime Evolution. To further assess STSW performance, we conduct a runtime analysis to understand the computational cost associated with different configurations. We again choose uniform distribution and $vMF(\mu, \kappa)$ where $\kappa = 10$ as our source and target distribution and use STSW to measure distance between these two probabilities. All experiments are repeated 20 times with default parameters set to $L = 200$ trees, $k = 10$ lines and $N = 500$ samples, unless otherwise stated.

We vary the number of trees $L \in \{200, 400, 500, 750, 900, 1000, 1250, 1500, 1750, 2000\}$ in Figure 9a, adjust the number of lines k across $\{5, 10, 25, 50, 100, 150, 200, 300, 500, 750, 1000\}$ in Fig-

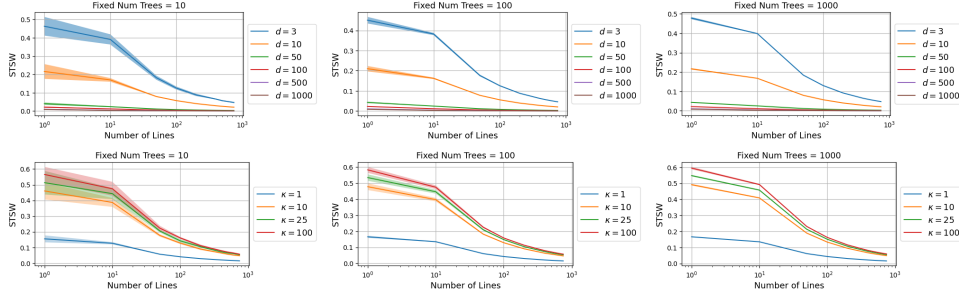


Figure 7: Evolution of STSW between two distributions w.r.t number of lines $k \in \{1, 10, 50, 100, 200, 400, 500, 600, 700, 750\}$.

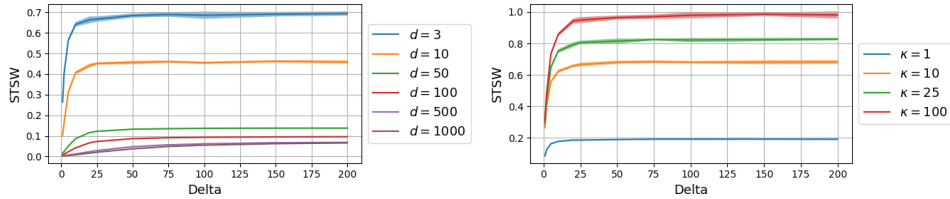


Figure 8: Evolution of STSW between two distributions w.r.t $\zeta \in \{1, 2, 5, 10, 20, 25, 50, 75, 100, 150, 200\}$

ure 9b and change the number of samples N within $\{500, 1000, 3000, 5000, 7000, 8000, 10000\}$ in Figure 9c. We note that the runtime of STSW scales linearly with these parameters.

B.3 GRADIENT FLOW

The probability density function of the von Mises-Fisher distribution with mean direction $\mu \in \mathbb{S}^d$ is given by:

$$f(x; \mu, \kappa) = C_d(\kappa) \exp(\kappa \mu^T x)$$

where $\kappa > 0$ is concentration parameter and the normalization constant $C_d(\kappa) = \frac{\kappa^{d/2-1}}{(2\pi)^{p/2} I_{p/2-1}(\kappa)}$

Our target distribution, 12 vMFs with 2400 samples (200 per vFM), have $\kappa = 50$ and

$$\begin{aligned} \mu_1 &= (-1, \phi, 0), & \mu_2 &= (1, \phi, 0), & \mu_3 &= (-1, -\phi, 0), & \mu_4 &= (1, -\phi, 0) \\ \mu_5 &= (0, -1, \phi), & \mu_6 &= (0, 1, \phi), & \mu_7 &= (0, -1, -\phi), & \mu_8 &= (0, 1, -\phi) \\ \mu_9 &= (\phi, 0, -1), & \mu_{10} &= (\phi, 0, 1), & \mu_{11} &= (-\phi, 0, -1), & \mu_{12} &= (-\phi, 0, 1) \end{aligned}$$

where $\phi = \frac{1 + \sqrt{5}}{2}$. The projected gradient descent as described in (Bonet et al., 2022):

$$\begin{cases} x^{(k+1)} = x^{(k)} - \gamma \nabla_{x^{(k)}} \text{STSW}(\hat{\mu}_k, \nu), \\ x^{(k+1)} = \frac{x^{(k+1)}}{\|x^{(k+1)}\|_2}, \end{cases}$$

Setup. We fix $L = 200$ trees and $k = 5$ lines. For the rest, we use $L = 1000$ projections. As in the original setup, ARI-S3W (30) has 30 rotations with a pool size of 1000 while RI-S3W (1) and RI-S3W (5) have 1 and 5 rotations respectively. We train with Adam (Kinga et al., 2015) optimizer $lr = 0.01$ over 500 epochs and an additional $lr = 0.05$ for SSW.

Results. As seen from Table 1 and Figure 10, STSW provides better results in log 2-Wasserstein distance and NLL, while also being efficient in terms of both runtime and convergence speed.

We perform additional experiments on the most informative sliced methods including MAX-STSW, MAX-SSW, and MAX-SW. We present in Table 5 the results after training for 1000 epochs with

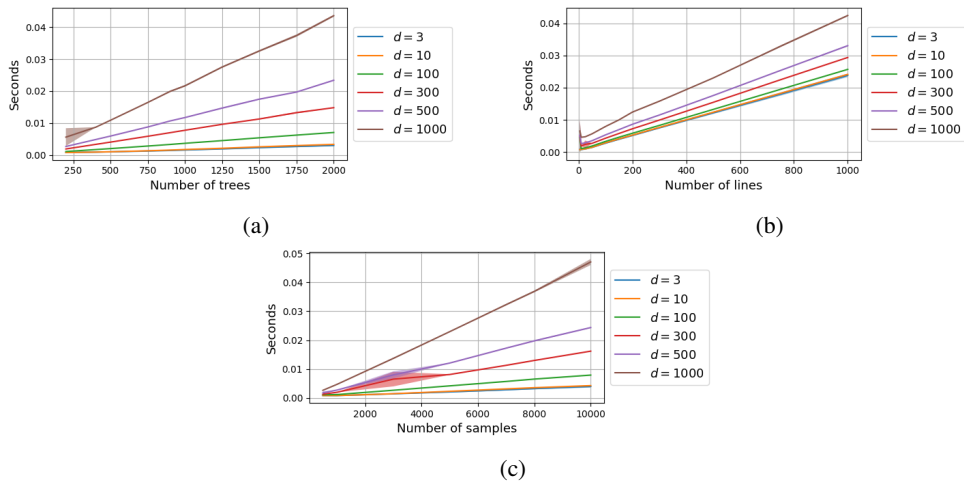


Figure 9: Runtime of STSW w.r.t number of trees, lines and samples

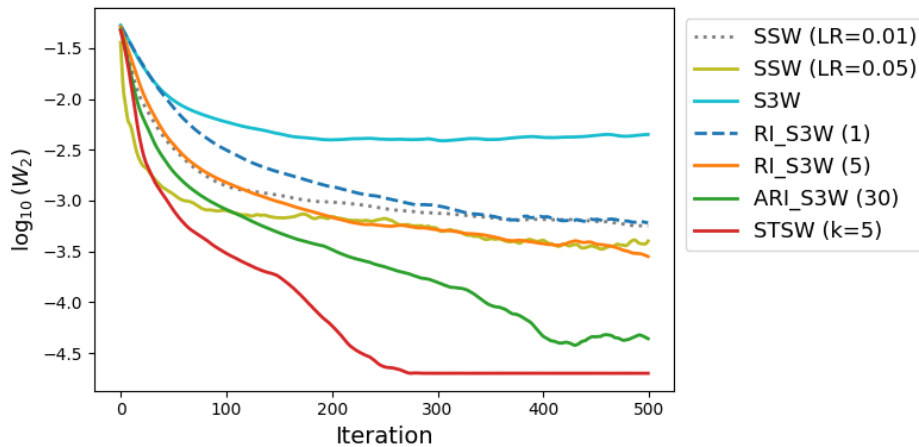


Figure 10: Log 2-Wasserstein distance between source and target distributions

a learning rate $LR = 0.01$. Each experiment is repeated 10 times. Figure 11 illustrates the log 2-Wasserstein distance between the source and target distribution during training. We observe that MAX-STSW performs better than others.

B.4 SELF-SUPERVISED LEARNING

Encoder. Consistent with the setup in (Bonet et al., 2022; Tran et al., 2024a), we train a ResNet18 (He et al., 2016) on CIFAR-10 (Krizhevsky, 2009) data for 200 epochs using a batch size of 512. We use SGD as our optimizer with initial $lr = 0.05$ a momentum 0.9, and a weight decay 10^{-3} . The standard data augmentations used to generate positive pairs are similar to prior works (Wang & Isola, 2020; Bonet et al., 2022; Tran et al., 2024a) which include resizing, cropping, horizontal flipping, color jittering, and random grayscale conversion.

We set $L = 200$ trees and $k = 20$ lines for STSW and fix $L = 200$ projections for all other sliced distances. $N_R = 5$ and a pool size of 100 are used for RI-S3W and ARI-S3W as in Tran et al. (2024a). For settings of the regularization coefficient, please refer to Table 6.

Linear Classifier. A linear classifier is then trained on feature representations from the pre-trained encoder. Similar to Bonet et al. (2022), we train it for 100 epochs using the Adam (Kinga et al., 2015) optimizer with a learning rate of 10^{-3} , a weight decay of 0.2 at epoch 60 and 80.

Table 5: Learning target distribution 12 vFMs, trained for 1000 epochs and averaged over 10 runs.

Method	$\log W_2 \downarrow$	NLL \downarrow
MAX-SW	-3.10 ± 0.06	-4959.14 ± 12.22
MAX-SSW	-2.76 ± 0.02	-4868.78 ± 60.51
MAX-STSW	-3.19 ± 0.03	-5007.72 ± 16.34

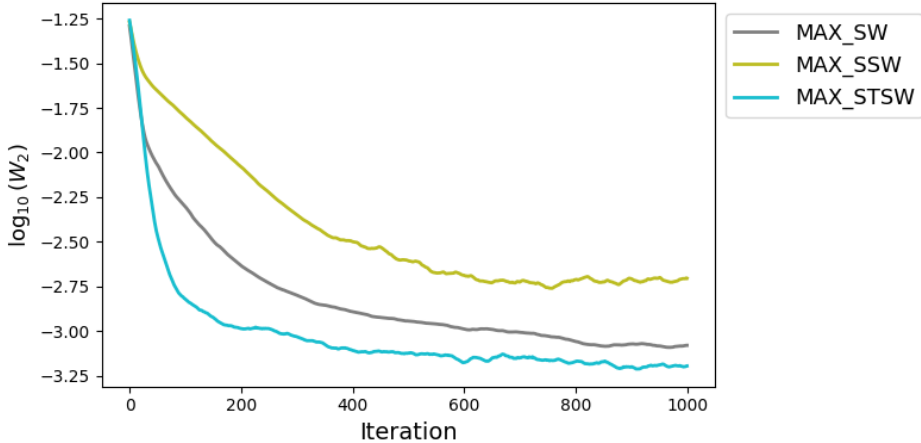


Figure 11: Log 2-Wasserstein distance between source and target distributions

Results. We report in Table 2 the best accuracy of the linear evaluation on features taken before and after projection on \mathbb{S}^d where $d = 9$. The visualizations of learned representations when $d = 2$ can be found in Figure 12.

B.5 EARTH DATA ESTIMATION

Similar to Bonet et al. (2022) and Tran et al. (2024a), we use an exponential mapping normalizing flows model consisting of 48 radial blocks with 100 components each, totaling 24000 parameters. The model is then trained with full batch gradient descent via Adam optimizer. Dataset details are provided in Table 7.

Setup. Our settings for STSW in this task are $L = 1000$ trees, $k = 100$ lines, and $\zeta = -100$. We use $lr = 0.05$ for STSW, S3W, RI-S3W and ARI-S3W and $lr = 0.1$ for SW and SSW. We train other sliced distances for 20,000 epochs as in the original setup while our STSW is only trained for 10,000 epochs.

Results. Table 3 highlights the competitive performance of STSW compared to the baseline methods. To further evaluate the efficiency of our approach, we compare the training time of STSW with that of the second-best performer, ARI-S3W, using the Fire dataset. Our findings show that STSW (2 hours 10 minutes) is twice as fast as ARI-S3W (4 hours 30 minutes). We also present in Figure 13 the normalized density maps of test data learned.

B.6 GENERATIVE MODELS

Setup. We use Adam (Kinga et al., 2015) optimizer with learning rate $lr = 10^{-3}$. We train with a batch size of 500 over 100 epochs using BCE loss as our reconstruction loss. We choose $L = 200$ trees and $k = 10$ lines for STSW. Following the same settings in Tran et al. (2024a), we fix $L = 100$ projections for others, $N_R = 5$ rotations for RI-S3W and ARI-S3W, and a pool size of 100 random rotations ARI-S3W. We use prior 10 vMFs, $\lambda = 1$ for STSW, $\lambda = 10$ for SSW, and $\lambda = 10^{-3}$ for SW and S3W variants.

Table 6: Regularization coefficient λ across various methods w.r.t projection on \mathbb{S}^d in Self-Supervised Learning task.

	STSW	SSW	SW	S3W variants
$d = 9$	$\lambda = 10.0$	$\lambda = 20.0$	$\lambda = 1.0$	$\lambda = 0.5$
$d = 2$	$\lambda = 10.0$	$\lambda = 20.0$	$\lambda = 1.0$	$\lambda = 0.1$

Table 7: Earth datasets.

	Earthquake	Flood	Fire
Train	4284	3412	8966
Test	1836	1463	3843
Data size	6120	4875	12809

Additional Results on MNIST. For quantitative analysis, we train the SWAE framework on MNIST and report the FID score in Table 8, along with the generated images in Figure 14. We follow the same settings as in Tran et al. (2024a), which use the latent prior $\mathcal{U}(S^2)$ and train the model with a batch size of 500 over 100 epochs. For STSW, we fix $L = 200$ trees and $k = 10$ lines with a learning rate $LR = 0.01$ and $\lambda = 1$. For other sliced methods, we use $L = 100$ projections and a learning rate $LR = 10^{-3}$, as described in Tran et al. (2024a). The FID scores are computed using 10,000 samples from the test set.

We use the same model architecture as specified in Tran et al. (2024a)

CIFAR-10 Model Architecture.

Encoder:

$$\begin{aligned}
 x \in \mathbb{R}^{3 \times 32 \times 32} &\rightarrow \text{Conv2d}_{32} \rightarrow \text{ReLU} \rightarrow \text{Conv2d}_{32} \rightarrow \text{ReLU} \\
 &\rightarrow \text{Conv2d}_{64} \rightarrow \text{ReLU} \rightarrow \text{Conv2d}_{64} \rightarrow \text{ReLU} \\
 &\rightarrow \text{Conv2d}_{128} \rightarrow \text{ReLU} \rightarrow \text{Conv2d}_{128} \rightarrow \text{Flatten} \\
 &\rightarrow \text{FC}_{512} \rightarrow \text{ReLU} \rightarrow \text{FC}_3 \\
 &\rightarrow \ell^2 \text{ normalization} \rightarrow z \in \mathbb{S}^2
 \end{aligned}$$

Decoder:

$$\begin{aligned}
 z \in \mathbb{S}^2 &\rightarrow \text{FC}_{512} \rightarrow \text{FC}_{2048} \rightarrow \text{ReLU} \\
 &\rightarrow \text{Reshape}(128 \times 4 \times 4) \rightarrow \text{Conv2dT}_{128} \rightarrow \text{ReLU} \\
 &\rightarrow \text{Conv2dT}_{64} \rightarrow \text{ReLU} \rightarrow \text{Conv2dT}_{64} \rightarrow \text{ReLU} \\
 &\rightarrow \text{Conv2dT}_{32} \rightarrow \text{ReLU} \rightarrow \text{Conv2dT}_{32} \rightarrow \text{ReLU} \\
 &\rightarrow \text{Conv2dT}_3 \rightarrow \text{Sigmoid}
 \end{aligned}$$

MNIST Model Architecture.

Encoder:

$$\begin{aligned}
 x \in \mathbb{R}^{28 \times 28} &\rightarrow \text{Conv2d}_{32} \rightarrow \text{ReLU} \rightarrow \text{Conv2d}_{32} \rightarrow \text{ReLU} \\
 &\rightarrow \text{Conv2d}_{64} \rightarrow \text{ReLU} \rightarrow \text{Conv2d}_{64} \rightarrow \text{ReLU} \\
 &\rightarrow \text{Conv2d}_{128} \rightarrow \text{ReLU} \rightarrow \text{Conv2d}_{128} \rightarrow \text{Flatten} \\
 &\rightarrow \text{FC}_{512} \rightarrow \text{ReLU} \rightarrow \text{FC}_3 \\
 &\rightarrow \ell^2 \text{ normalization} \rightarrow z \in \mathbb{S}^2
 \end{aligned}$$

Decoder:

$$z \in \mathbb{S}^2 \rightarrow \text{FC}_{512} \rightarrow \text{FC}_{512} \rightarrow \text{ReLU}$$

1566
 1567
 1568
 1569
 1570
 1571
 1572
 1573
 1574
 1575
 1576
 1577
 1578
 1579
 1580
 1581
 1582
 1583
 1584
 1585
 1586
 1587
 1588
 1589
 1590
 1591
 1592
 1593
 1594
 1595
 1596
 1597
 1598
 1599
 1600
 1601
 1602
 1603
 1604
 1605
 1606
 1607
 1608
 1609
 1610
 1611
 1612
 1613
 1614
 1615
 1616
 1617
 1618
 1619

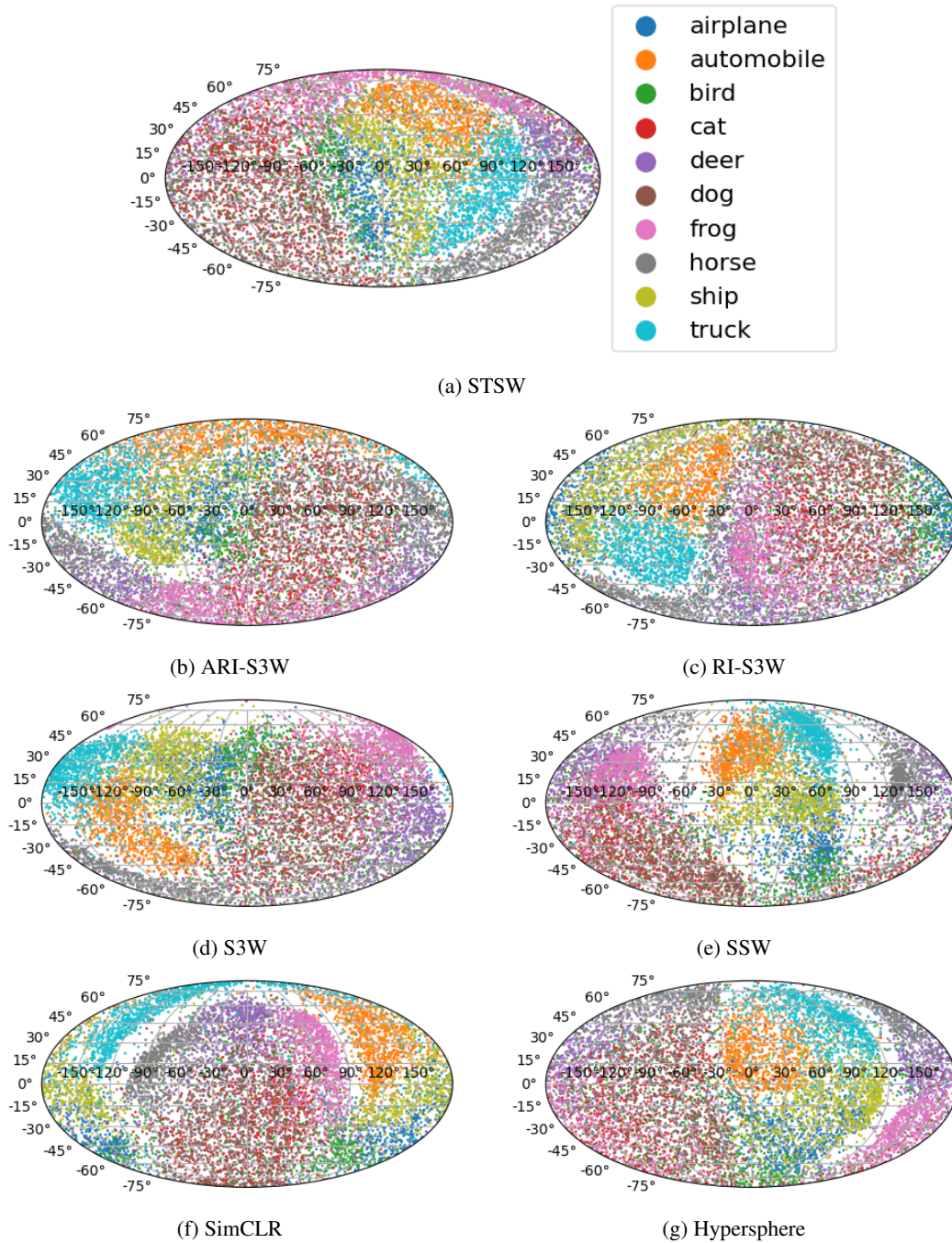


Figure 12: Distributions of CIFAR-10 validation set on \mathbb{S}^2 after pre-training.

→ Reshape($128 \times 2 \times 2$) → Conv2dT₁₂₈ → ReLU
 → Conv2dT₆₄ → ReLU → Conv2dT₆₄ → ReLU
 → Conv2dT₃₂ → ReLU → Conv2dT₃₂ → ReLU
 → Conv2dT₁ → Sigmoid

1620
 1621
 1622
 1623
 1624
 1625
 1626
 1627
 1628
 1629
 1630
 1631
 1632
 1633
 1634
 1635
 1636
 1637
 1638
 1639
 1640
 1641
 1642
 1643
 1644
 1645
 1646
 1647
 1648
 1649
 1650
 1651
 1652
 1653
 1654
 1655
 1656
 1657
 1658
 1659
 1660
 1661
 1662
 1663
 1664
 1665
 1666
 1667
 1668
 1669
 1670
 1671
 1672
 1673

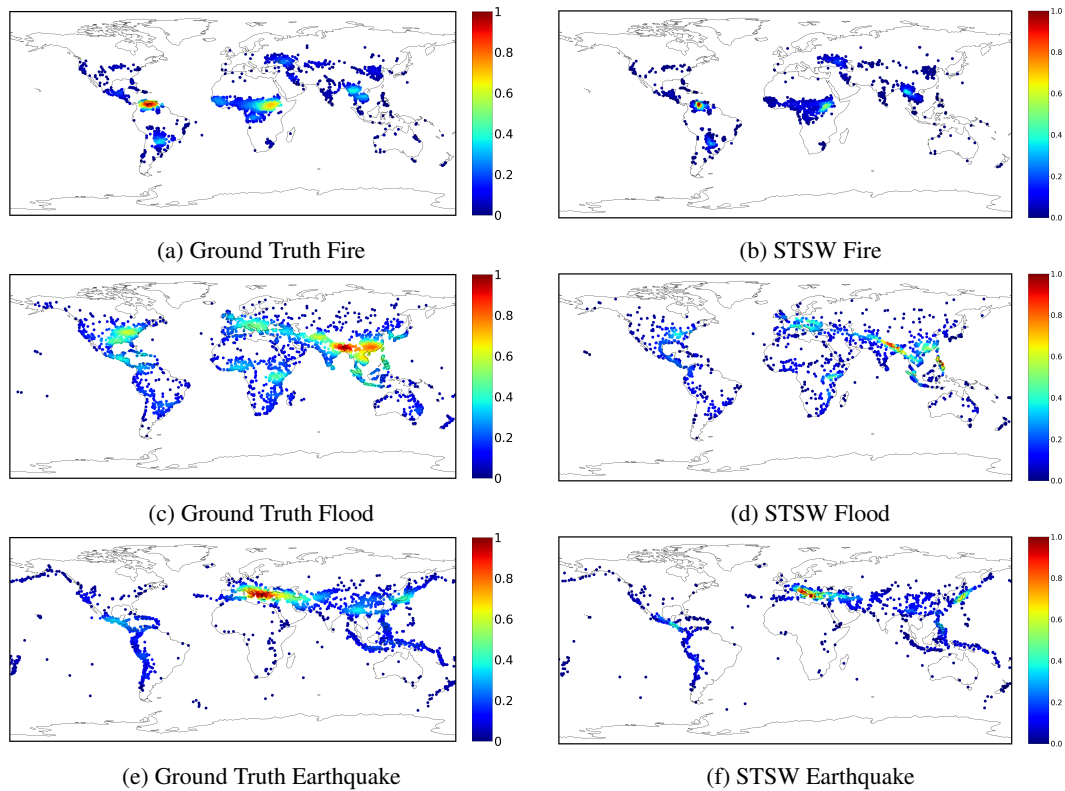


Figure 13: Density estimation on earth data. The left figures (ground truth) represent training data estimated with KDE. The right ones depict the normalized log likelihood of the trained models on test data.

Table 8: Average FID of 5 runs on MNIST.

Method	FID ↓
SW	73.35 ± 2.01
SSW	76.14 ± 2.73
S3W	75.55 ± 2.80
RI-S3W (10)	72.80 ± 3.39
ARI-S3W (30)	70.37 ± 2.58
STSW	69.16 ± 2.74

1674
 1675
 1676
 1677
 1678
 1679
 1680
 1681
 1682
 1683
 1684
 1685
 1686
 1687
 1688
 1689
 1690
 1691
 1692
 1693
 1694
 1695
 1696
 1697
 1698
 1699
 1700
 1701
 1702
 1703
 1704
 1705
 1706
 1707
 1708
 1709
 1710
 1711
 1712
 1713
 1714
 1715
 1716
 1717
 1718
 1719
 1720
 1721
 1722
 1723
 1724
 1725
 1726
 1727

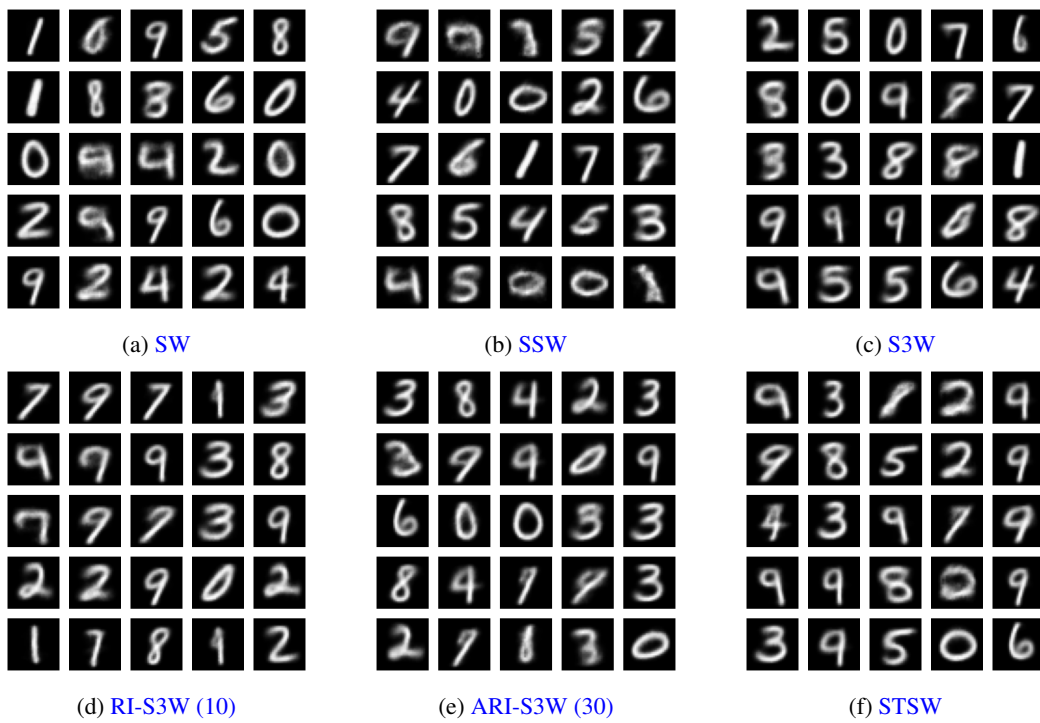


Figure 14: Generated images of different methods on MNIST of SWAE.